

# Astrophysical Shrapnel: Discriminating Among Near-Earth Stellar Explosion Sources of Live Radioactive Isotopes

Brian J. Fry and Brian D. Fields

*Department of Astronomy, University of Illinois, Urbana, IL 61801, USA*

John R. Ellis

*Theoretical Physics and Cosmology Group, Department of Physics, King's College London, London WC2R  
2LS, UK, and Theory Division, Physics Department, CERN, CH-1211 Geneva 23, Switzerland*

## ABSTRACT

We consider the production and deposition on Earth of isotopes with half-lives in the range  $10^5$  to  $10^8$  years that might provide signatures of nearby stellar explosions, extending previous analyses of Core-Collapse Supernovae (CCSNe) to include Electron-Capture Supernovae (ECSNe), Super-Asymptotic Giant Branch (SAGBs) stars, Thermonuclear/Type Ia Supernovae (TNSNe), and Kilonovae/Neutron Star Mergers (KNe). We revisit previous estimates of the  $^{60}\text{Fe}$  and  $^{26}\text{Al}$  signatures, and extend these estimates to include  $^{244}\text{Pu}$  and  $^{53}\text{Mn}$ . We discuss interpretations of the  $^{60}\text{Fe}$  signals in terrestrial and lunar reservoirs in terms of a nearby stellar ejection  $\sim 2.2$  Myr ago, showing that (i) the  $^{60}\text{Fe}$  yield rules out the TNSN and KN interpretations, (ii) the  $^{60}\text{Fe}$  signals highly constrain a SAGB interpretation but do not completely rule them out, (iii) are consistent with a CCSN origin, and (iv) are highly compatible with an ECSN interpretation. Future measurements could resolve the radioisotope deposition over time, and we use the Sedov blast wave solution to illustrate possible time-resolved profiles. Measuring such profiles would independently probe the blast properties including distance, and would provide additional constraints the nature of the explosion.

KCL-PH-TH/2014-16, LCTS/2014-15, CERN-PH-TH/2014-062

## 1. Introduction

The most violent stellar explosions are the sources of most of the heavy elements on Earth, and supernovae (SNe) in particular are estimated to occur at a rate of  $\sim 1 - 3$  per century in our Galaxy (e.g., Adams et al. 2013, and references therein). It is inevitable that, over the course of geological time, some such explosions will have occurred within  $\sim 100$  pc of the Earth, close enough to have deposited some ejecta on the Earth and Moon (e.g., Shklovskij 1969; Fields 2004, and references therein). Indeed, the Geminga pulsar located  $\sim 250$  pc away (Faherty et al. 2007) is the remnant of a SN explosion estimated to have occurred  $\sim 300$  kyr ago, and may be partly responsible for the low density of the interstellar medium (ISM) around the Solar System (Bignami & Caraveo 1996). Similarly,  $^{26}\text{Al}$  gamma-ray line emission and large-angle  $\text{H}\alpha$  filaments suggest a SN towards the Antlia constellation  $60 - 240$  pc away (McCullough et al. 2002); if this event created a neutron star associated with the high-proper-motion pulsar PSR J0630-2834, then the explosion occurred about 1.2 Myr ago at about 140 pc (Tetzlaff et al. 2013). The question then arises whether some closer astrophysical explosion might have left detectable traces on the Earth itself in the form of geological

isotope anomalies. Moreover, with a closer astrophysical explosion, the possibility for biological damage, even a mass extinction arises (for recent references, see, e.g., Melott & Thomas 2011; Beech 2011; Dartnell 2011; Atri & Melott 2014).

Discussions of this possibility date back to the pioneering study of Alvarez et al. (1980). These authors discovered an iridium anomaly associated with the Cretaceous-Tertiary transition that they argued could not, in fact, be associated with a SN explosion, but instead with a giant impact. Subsequently, Ellis et al. (1996) surveyed possible isotope signatures of a nearby SN explosion, including  $^{26}\text{Al}$ ,  $^{53}\text{Mn}$ ,  $^{60}\text{Fe}$ , and  $^{244}\text{Pu}$ . Motivated by this study, Knie et al. (1999) searched for an anomaly in the  $^{60}\text{Fe}$  abundance in a deep-ocean ferro-manganese (Fe-Mn) crust, and found one that appeared  $\sim 2.2$  Myr ago. Although primordial Solar System composition shows enrichment from extra-solar origins, to our knowledge, this is the first such specific extra-solar event to be identified. Following the Knie et al. (1999) discovery, its interpretation was discussed in Fields & Ellis (1999) and possible corroborating isotope signatures were discussed in Fields et al. (2005). Benítez et al. (2002) proposed that the event arose in the Sco-Cen OB association, which was  $\sim 130$  pc away at the time of the  $^{60}\text{Fe}$ -producing event. Fields et al. (2008) presented hydrodynamic models for the SN blast impact with the solar wind, and Athanassiadou & Fields (2011) highlighted the importance of the ejecta condensation into dust grains.

The  $^{60}\text{Fe}$  signal has subsequently been confirmed in another Fe-Mn crust sample (Knie et al. 2004; Fitoussi et al. 2008) and in lunar regolith (Cook et al. 2009; Fimiani et al. 2012, 2014), but no other accompanying isotope anomaly has been found in studies of  $^{26}\text{Al}$  abundances (Feige et al. 2013). Searches for  $^{244}\text{Pu}$  have produced just a single count, albeit with no stable isobar background (Wallner et al. 2000, 2004).

In this paper, we broaden our previous analyses in four ways. In a first step, we provide yields for isotopes from the CCSNe considered previously and extend our analysis to include the cases of ECSNe, TNSNe (also known as a Type Ia SN), KNe (also known as Neutron Star Mergers), and SAGBs, which have not been considered previously in this context. For this paper, we distinguish between ECSNe and the more massive CCSNe since there are qualitative differences in the collapse and explosion mechanism as well as nucleosynthesis of these two classes. Secondly, we revisit the formalism surrounding the deposition calculations, including the impact and some geology of the uptake factor, and also the possibility of using sediments to get time-resolved signals and give predictions for these profiles. We also discuss the filtering processes impacting the transport of the signal via dust. Next, we discuss the compatibility between the terrestrial and lunar evidence for a  $^{60}\text{Fe}$  anomaly, and we also analyze the existing limits on the  $^{26}\text{Al}$  abundance from samples bracketing the  $^{60}\text{Fe}$  anomaly. In combination with these previous steps, as a fourth and final step, we survey the possible interpretations of the  $^{60}\text{Fe}$  anomaly and make predictions for upcoming measurements.

We find that a TNSN and a KN would yield too little  $^{60}\text{Fe}$ , and can be ruled out as possible sources for the Knie et al. (2004)  $^{60}\text{Fe}$  signal. Additionally, we find a SAGB source constrained, but not eliminated due to uncertainty in the Local Bubble’s magnetic field and the location of a possible SAGB source. CCSNe from our set of masses and ECSNe can not be ruled out based on the available measurements.

## 2. Progenitors and Delivery to the Solar System

Previous papers have focused on CCSNe as the likeliest progenitor for the  $^{60}\text{Fe}$  signal. However, there are other astrophysical ejections that are thought to produce  $^{60}\text{Fe}$  but have not been considered previously. These include TNSNe, ECSNe, KNe, and SAGBs. Table 1 summarizes the yields for possible CCSNe,

ECSNe, and SAGBs progenitors as used in our model calculations; yields are expressed in units of  $M_\odot$ .

Table 1: Ejected Masses for Various Radioactive Isotopes, in  $M_\odot$

Progenitor	15- $M_\odot$ CCSN <sup>a</sup>	19- $M_\odot$ CCSN <sup>a</sup>	20- $M_\odot$ CCSN <sup>a</sup>	21- $M_\odot$ CCSN <sup>a</sup>	25- $M_\odot$ CCSN <sup>a</sup>	8-10- $M_\odot$ ECSN <sup>b</sup>
<sup>26</sup> Al	$2.6 \times 10^{-5}$	$3.2 \times 10^{-5}$	$3.0 \times 10^{-5}$	$4.6 \times 10^{-5}$	$7.0 \times 10^{-5}$	$4.4 \times 10^{-8}$
<sup>53</sup> Mn	$1.8 \times 10^{-4}$	$2.1 \times 10^{-4}$	$1.3 \times 10^{-4}$	$2.3 \times 10^{-4}$	$3.6 \times 10^{-4}$	$1.1 \times 10^{-6}$
<sup>60</sup> Fe	$6.6 \times 10^{-5}$	$1.1 \times 10^{-4}$	$3.6 \times 10^{-5}$	$2.5 \times 10^{-5}$	$1.5 \times 10^{-4}$	$3.6 \times 10^{-5}$
<sup>41</sup> Ca	$4.3 \times 10^{-6}$	$2.7 \times 10^{-5}$	$4.3 \times 10^{-4}$	$6.9 \times 10^{-6}$	$3.2 \times 10^{-5}$	$2.0 \times 10^{-7}$
<sup>93</sup> Zr	$1.3 \times 10^{-8}$	$4.7 \times 10^{-8}$	$9.8 \times 10^{-9}$	$5.9 \times 10^{-8}$	$1.5 \times 10^{-7}$	N/A <sup>d</sup>
<sup>97</sup> Tc	$4.8 \times 10^{-11}$	$4.2 \times 10^{-11}$	$1.9 \times 10^{-10}$	$1.3 \times 10^{-10}$	$8.3 \times 10^{-11}$	N/A <sup>d</sup>
<sup>107</sup> Pd	$4.1 \times 10^{-10}$	$8.4 \times 10^{-10}$	$4.6 \times 10^{-10}$	$1.4 \times 10^{-9}$	$1.4 \times 10^{-9}$	N/A <sup>d</sup>
<sup>146</sup> Sm	$3.9 \times 10^{-10}$	$6.3 \times 10^{-12}$	$3.4 \times 10^{-10}$	$8.5 \times 10^{-10}$	$1.2 \times 10^{-9}$	N/A <sup>d</sup>
<sup>182</sup> Hf	$1.4 \times 10^{-10}$	$1.5 \times 10^{-9}$	$2.5 \times 10^{-10}$	$5.5 \times 10^{-10}$	$4.3 \times 10^{-10}$	N/A <sup>d</sup>
<sup>244</sup> Pu <sup>c</sup>	$2.0 \times 10^{-11}$	$2.2 \times 10^{-10}$	$3.7 \times 10^{-11}$	$8.1 \times 10^{-11}$	$6.3 \times 10^{-11}$	N/A <sup>d</sup>
Progenitor	6.5- $M_\odot$ SAGB <sup>e</sup>	7.0- $M_\odot$ SAGB <sup>e</sup>	7.5- $M_\odot$ SAGB <sup>e</sup>	8.0- $M_\odot$ SAGB <sup>e</sup>	8.5- $M_\odot$ SAGB <sup>e</sup>	9.0- $M_\odot$ SAGB <sup>e</sup>
<sup>26</sup> Al	$5.0 \times 10^{-6}$	$5.0 \times 10^{-6}$	$5.0 \times 10^{-6}$	$8.0 \times 10^{-6}$	$1.0 \times 10^{-5}$	$1.1 \times 10^{-5}$
<sup>53</sup> Mn	0	0	0	0	0	0
<sup>60</sup> Fe	$5.0 \times 10^{-6}$	$3.0 \times 10^{-6}$	$4.0 \times 10^{-6}$	$9.0 \times 10^{-6}$	$1.4 \times 10^{-5}$	$1.4 \times 10^{-5}$

Note: In addition to the cited CCSN yields from Rauscher et al. (2002), <sup>26</sup>Al and <sup>60</sup>Fe yields from Limongi & Chieffi (2006) (11-120  $M_\odot$ ) were investigated as well. These did not show any additional features beyond those shown with the Rauscher et al. (2002) yields.

<sup>a</sup> - S15, S19, S20, S21, and S25 Models respectively, Rauscher et al. (2002)

<sup>b</sup> - “unchanged” configuration, Wanajo et al. (2013)

<sup>c</sup> - <sup>244</sup>Pu yields calculated as outlined in Fields et al. (2005) but using Rauscher et al. (2002) <sup>182</sup>Hf yields

<sup>d</sup> - r-process yields for ECSN are not available at present although Wanajo et al. (2013) stated that ECSN may produce some weak r-process elements

<sup>e</sup> - Doherty et al. (2013)

## 2.1. Supernovae

SNe include both CCSNe and TNSNe; CCSNe are the results of massive stars completing Fe/Ni fusion in their cores and collapsing under the influence of gravity whereas TNSNe result from runaway nuclear fusion in a C-O white dwarf near its Chandrasekhar limit. Both types have similar explosive energies and modes of transporting ejecta. However, although known to be sources of stable iron isotopes, TNSNe are calculated to produce relatively little <sup>60</sup>Fe, namely  $\sim 2.3 \times 10^{-9} M_\odot$ , according to the W7 Type Ia Model of Nomoto, Thielemann & Yokoi (1984). ECSNe form a special subcategory of CCSNe with significantly different radioactive isotope yields. While the <sup>60</sup>Fe yields for CCSNe and ECSNe are similar ( $\sim 10^{-6} - 10^{-3} M_\odot$ , Rauscher et al. 2002; Limongi & Chieffi 2006), their yields for other isotopes (e.g., <sup>26</sup>Al and <sup>53</sup>Mn) are vastly different (Wanajo et al. 2013). For the purposes of this paper, ECSNe will refer to SNe from 8 – 10  $M_\odot$  stars, CCSNe will refer to SNe with progenitor masses  $> 10 M_\odot$ , and SNe will refer to

CCSNe, ECSNe, and TNSNe. It should be noted that the yields for  $^{244}\text{Pu}$  were calculated using the same method from Fields et al. (2005); the proportions of  $r$ -process elements are generally consistent to that found in metal-poor globular clusters and in the Sun. In this paper, however, the yields for  $^{244}\text{Pu}$  were based on the yields for  $^{182}\text{Hf}$  from Rauscher et al. (2002) using the ratios given in Fields et al. (2005).

SNe can show large variations in their isotope yields. TNSN  $^{60}\text{Fe}$  yields show variations over several orders of magnitude ( $\sim 10^{-18} - 10^{-7} M_{\odot}$ ) due to variations in the number and location of ignition points and the transition from deflagration to detonation (Seitenzahl et al. 2013).<sup>1</sup> CCSNe/ECSNe yields are highly dependent on a number of factors including when different layers are mixed. This can be seen in the variations of yields from one mass to another (Rauscher et al. 2002). The yields within a given mass are also subject to uncertainties in nuclear reaction rates ( $3\text{-}\alpha$  and  $^{12}\text{C}(\alpha,\gamma)^{16}\text{O}$ ) which can lead to an almost order of magnitude shift in the production of  $^{26}\text{Al}$  and  $^{60}\text{Fe}$  (Tur et al. 2010). In §6, Figure 3, we show the calculated distances with uncertainties indicated by dashed lines for a factor of 5 variation in the  $^{60}\text{Fe}$  yield for each CCSN/ECSN type.

Fiducial parameters for the explosions and the interstellar medium are chosen as follows: We assume CCSNe and TNSNe deposit  $E_{\text{CCSN}} \ \& \ E_{\text{TNSN}} = 10^{51}$  ergs into their ejecta, while ECSNe deposit  $E_{\text{ECSN}} = 10^{50}$  ergs (Wanaajo et al. 2009). Because the Local Bubble shows evidence of multiple SN explosions, we will assume that if a SN were the source of the  $^{60}\text{Fe}$  signal, it would be the most recent SN, meaning the SN occurred in an already depleted ISM, but not as depleted as the current density of the Local Bubble (i.e.,  $n_{\text{Average ISM}} = 1.0 \text{ cm}^{-3} > n_{\text{ISM}} > n_{\text{Local Bubble}} = 0.005 \text{ cm}^{-3}$ ). Therefore, we estimated a SN would have occurred in an ISM of density,  $n_{\text{ISM}} = 0.1 \text{ cm}^{-3}$ , temperature,  $T = 8000 \text{ K}$ , and sound speed,  $c_s = 10 \text{ km s}^{-1}$  (i.e., approximate values for the Local Cloud, Fields et al. 2008).

## 2.2. Kilonovae

KNe are thought to result from Neutron Star-Neutron Star (NS-NS) or in some cases Neutron Star-Black Hole (NS-BH) mergers (Li & Paczyński 1998; Metzger et al. 2010; Tanvir et al. 2013). For this paper, we only consider the KN explosion’s lower-energy, spherical/toroidal ejection and not its highly beamed gamma-ray burst jet. The rapid decompression and ejection of neutron-rich NS matter makes these events a natural site for the  $r$ -process (Lattimer & Schramm 1974; Symbalisty & Schramm 1982). While KNe are less energetic than SNe ( $E_{\text{KN}} = 10^{49}$  ergs, Goriely et al. 2011), we will consider a possible KN source of the  $^{60}\text{Fe}$  signal as occurring in the same ISM conditions as a SN. However, given the axisymmetric nature of NS-NS mergers, we will not apply the same constraints to KNe as SNe, but will instead evaluate KNe with respect to isotope yields and frequency.

While there has been some modeling of KN yields, none we are aware of have specifically stated a yield for  $^{60}\text{Fe}$ . However, it is possible to determine an upper limit on the range for a KN. In Goriely et al. (2011), they list mass fractions for every atomic number up to  $\sim 200$  for a NS-NS merger with a total merger mass of  $2.7 M_{\odot}$ . If we assume all of the isotopes with  $A = 60$  are in the form of  $^{60}\text{Fe}$  ( $M_{\text{ej,total}} = 10^{-3} - 10^{-2}$ ,  $X_{^{60}\text{Fe}} = 10^{-5}$ ) then the upper limit to the mass of ejecta in  $^{60}\text{Fe}$  is  $10^{-7} M_{\odot}$ .

---

<sup>1</sup>We adopt a fiducial TNSN  $^{60}\text{Fe}$  yield of  $\sim 10^{-9} M_{\odot}$ , which is consistent with the classic W7 result (Nomoto, Thielemann & Yokoi 1984) and is larger than almost all Seitenzahl et al. (2013) models.

### 2.3. Super-Asymptotic Giant Branch Stars

SAGBs ( $6.5 - 9 M_{\odot}$ ) are post-main sequence stars that produce large amounts of dust (see, e.g., Ventura et al. 2012) and have strong winds ( $\sim 30 \text{ km s}^{-1}$ ) capable carrying dust great distances. SAGBs produce  $10^{-6} - 10^{-5} M_{\odot}$  of  $^{60}\text{Fe}$  (Doherty et al. 2013), but are distinguishable from SNe in that they produce practically no  $^{53}\text{Mn}$  (Wasserburg et al. 2006; Fimiani et al. 2014). We note that SAGB yields are subject to an uncertainty in the onset of the super-wind phase (Doherty et al. 2013); a delayed onset results in generally increased yields. The implication for distance is shown with dashed error bars on SAGB results in §6, Figure 3. In contrast to SNe, we do not expect a SAGB wind to affect the density of the Local Bubble appreciably, and we assume that a SAGB source for the  $^{60}\text{Fe}$  signal would have occurred in an ISM like that found in the Local Bubble today (i.e.,  $n_{\text{ISM}} = 0.005 \text{ cm}^{-3}$ , temperature,  $T = 10^6 \text{ K}$ , and sound speed,  $c_s = 100 \text{ km s}^{-1}$ ). Finally, we assume the initial velocity of the SAGB grains to be:  $v_{\text{grain},0} = 30 \text{ km s}^{-1}$ .

### 2.4. Dust Transport to the Solar System

Regardless of the source, any  $^{60}\text{Fe}$  arriving in the Solar System will need to be in the form of dust. Fields et al. (2008) showed that the solar wind will keep any gaseous isotopes from reaching the Earth (unless a SN is sufficiently close, but this will be used as a constraint later in §3.1 and §6). We assume that the dust grains are spherical and select as our fiducial values for dust grains: density,  $\rho_{\text{grain}} = 3.5 \text{ g cm}^{-3}$  (an average value for silicates), radius,  $a = 0.2 \mu\text{m}$  (this selection is based on discussion in §4.2), and voltage,  $\mathcal{V} = 0.5 \text{ V}$ . Departures from these values will be specifically stated.

## 3. Formalism

In order to identify the most likely progenitor, we will attempt to constrain the source and its allowable distances using the measured  $^{60}\text{Fe}$  fluence and calculated yields. In the future, with additional measurements of other isotopes, we can use the other isotope yields to constrain the source using the observed isotope to  $^{60}\text{Fe}$  ratio.

Several previous works have presented the formalism for calculating deposited material from a SN (Ellis et al. 1996; Fields & Ellis 1999; Fields et al. 2005). These works focused primarily on short ranges (SN distances,  $D \sim 10 \text{ pc}$ ) and on the isotope  $^{60}\text{Fe}$ . For such short distances, the losses due to decay of live radionuclides en route from the SN to Earth amount to  $\lesssim 1\%$  and can be ignored. At greater ranges ( $D \sim 100 \text{ pc}$ ) and for shorter-lived isotopes (in particular,  $^{26}\text{Al}$  with  $\tau_{1/2,^{26}\text{Al}} = 0.717 \text{ Myr}$ ) decays en route become a significant issue. Accounting for this, the observed fluence today,  $\mathcal{F}_{\text{obs},i}$ , for each isotope,  $i$ , in atoms per area on the surface of the Earth within a given substance (e.g., crust, sediment, etc.) becomes:

$$\mathcal{F}_{\text{obs},i} = \left(\frac{1}{4}\right) \left(\frac{M_{\text{ej},i}}{4\pi D^2 A_i m_u}\right) U_i f_i e^{-(t_{\text{arr}} + t_{\text{travel}})/\tau_i} \quad (1)$$

where  $M_{\text{ej},i}$  is the mass of the ejecta by isotope,  $D$  is the distance from the progenitor to Earth,  $A_i$  is the atomic number of the isotope,  $m_u$  is the atomic mass unit,  $t_{\text{arr}}$  is the time from today since the ejecta arrived at Earth, and  $t_{\text{travel}}$  is the time the ejecta traveled from the source to Earth. Also,  $\tau_i$  is the mean lifetime of the isotope ( $\tau_i = \tau_{1/2,i}/\ln 2$ ).

The uptake,  $U_i \equiv (\text{Amount Collected})/(\text{Amount Deposited})$ , is the fraction of the isotope deposited on a surface that is collected by that material. The quantity is dimensionless, and ranges from 1 (the material

collects 100% of deposited element) to 0 (the material collects 0% of deposited element).<sup>2</sup> It is further discussed in §4.1. Additionally, the dust fraction,  $f_i$ , is the amount of the isotope in the form of dust that arrives at Earth (§4.2). It is similar to uptake in that it is also dimensionless and ranges from 1 (all of the isotope is in the form of dust and reaches Earth) to 0 (none of the isotope is dust and/or reaches Earth). There is a factor of (1/4) from the ratio of the Earth’s cross sectional to surface areas, because it is assumed material is distributed evenly over Earth’s entire surface through collisional accretion only. Equation (1) also assumes an isotropic dispersal of material from the source ( $4\pi D^2$  factor for spherical distribution), that no additional isotopes are created after the ejection from the progenitor, and that the ejected material passes through a homogeneous ISM.

There are three other fluence quantities that appear in the literature: “decay-corrected” fluence, “surface” fluence, and “interstellar” fluence. The decay-corrected or arrival fluence,  $\mathcal{F}_{\text{arr},i}$ , is the total number of atoms per area that would have been measured at the time the signal arrived. It is calculated by correcting our previous description of fluence (see Equation (1)) for radioactive decay since the isotope was deposited  $\mathcal{F}_{\text{arr},i} = e^{t_{\text{arr}}/\tau_i} \mathcal{F}_{\text{obs},i}$ . The surface fluence or global mean fluence,  $\mathcal{F}_{\text{surface},i}$ , is the total number of atoms per area that arrive at the surface of the Earth regardless of what substance they might be incorporated into, and is found by dividing the decay-corrected fluence by the uptake (i.e.,  $\mathcal{F}_{\text{surface},i} = \mathcal{F}_{\text{arr},i}/U_i$ ). It will be used in §5 and §6 and will be specifically stated when used. The interstellar fluence,  $\mathcal{F}_{\text{interstellar},i}$ , also appears in the literature (e.g., Fitoussi et al. 2008; Cook et al. 2009), namely the number of atoms per area on the surface of the spherical shock front. It is related to the surface fluence by a factor of 4, the ratio of Earth’s cross section to surface area (i.e.,  $\mathcal{F}_{\text{interstellar},i} = 4\mathcal{F}_{\text{surface},i}$ ). Interstellar fluence will not be used in this paper, but the reader should be aware of the distinction when reviewing the literature.

In order to find the time delay,  $t_{\text{travel}}$ , from ejection to deposition on Earth, we must account for the propagation of the ejection through the intervening ISM, which depends on the progenitor. SNe transmit material via an explosive shock, whereas SAGBs use a wind-driven ejection. In the case of SNe, we will assume that the shock has transitioned from the free-expansion phase into the adiabatic/energy-conserving phase. For SAGBs, we will assume dust has been blown by winds from the star and experiences drag as it travels to Earth.

### 3.1. SN Expansion Profile and Constraints

For SNe in the adiabatic/energy-conserving phase, the shock follows a self-similar or Sedov-Taylor expansion profile. With the explosion at time  $t = 0$ , a shock is launched with radius,  $R_{\text{SN}}$ , at elapsed time,  $t$ , given by:

$$R_{\text{SN}} = \xi_0 \left( \frac{E_{\text{SN}} t^2}{\rho_{\text{ISM}}} \right)^{1/5} \quad (2)$$

for a SN explosion depositing energy  $E_{\text{SN}}$  into the ejecta, propagating into a local interstellar medium of density  $\rho_{\text{ISM}} = m_u n_{\text{ISM}}$ . The quantity  $\xi_0$  is a dimensionless constant that is of order unity for  $\gamma = 5/3$  using the derivation in Zel’dovich & Raizer (1967). Thus the time interval to traverse distance,  $D$ , is:

$$t_{\text{travel,SN}} = \left( \frac{D}{\xi_0} \right)^{5/2} \left( \frac{\rho_{\text{ISM}}}{E_{\text{SN}}} \right)^{1/2} \quad (3)$$

---

<sup>2</sup>It is possible to have  $U_i > 1$  if, for example, a marine sample can chemically scavenge the element of interest so efficiently that it collects more than the amount deposited in the water column directly over the sample.

where we have assumed a uniform ISM density. While we know this is a crude approximation (see e.g., Abt 2011), deviations from the uniform case would be encoded into the signal and could be determined if the signal is time-resolved (for examples of non-uniform media, see Book 1994). We use the uniform ISM case as a baseline.

The density versus radius profile for a SN signal may be approximated by a “saw-tooth” profile. As will be described in greater detail in §3.3, §3.4, and Appendix B, measurements in sediment open the possibility to making time-resolved fluence measurements. A saw-tooth pattern gives a better approximation of the more exact Sedov solution than a uniform shell profile. The saw-tooth pattern reaches its maximum density value at the outer edge of the shock, then decreases linearly to a fraction of the total shock radius,  $\epsilon$ , where the density is zero from that point to the center of the remnant. See Appendix B for a comparison of the exact Sedov, saw-tooth, and uniform shell profiles.

Possible SNe will be constrained by an inner “kill” distance and an outer “fadeaway” distance. The kill distance is the range at which a SN can occur and create extinction-level disruptions to the Earth’s biosphere. The primary mechanism for a SN to accomplish this is for ionizing radiation (i.e., gamma-rays, hard X-rays, and cosmic-rays) to destroy  $O_3$  and  $N_2$  in the atmosphere producing nitric oxides ( $NO_y$ ) and leaving the biosphere vulnerable to UVB rays from the Sun (first described by Shklovskii & Sagan 1966, described in detail by Ruderman 1974, and updated by Ellis & Schramm 1995). This can be accomplished either by direct exposure (i.e., an X-ray flash from the SN) or by a “descreening” boost in cosmic-ray flux.<sup>3</sup> Gehrels et al. (2003) calculated a kill distance  $R_{\text{kill}} \lesssim 8$  pc for the direct exposure case using the galactic gamma-ray background and SN rates, although, as pointed out by Melott & Thomas (2011), this is probably an underestimation based on more recent rate estimations. This work was expanded upon by Ejzak et al. (2007) and Thomas et al. (2008) to include X-rays and showed that for exposure durations up to  $10^8$  s, the effects on the biosphere were the same and that the critical value for an extinction-level SN event was an energy fluence of  $10^8$  ergs  $\text{cm}^{-2}$  (not to be confused with the description of fluence used throughout the rest of this paper). As noted in Melott & Thomas (2011), these direct exposure calculations use SN rate and photon and cosmic-ray emission information that are improving, but still subject to large uncertainties.

Here we calculate the kill distance using the descreening case described in Fields et al. (2008); it yields the same range as the direct exposure calculations, and is scalable to the energy of the SN,  $E_{\text{SN}}$ . The descreening kill distance is the range at which a SN can occur and its shock will penetrate the Solar System to within 1 AU of the Sun. It is determined by setting the solar wind pressure,  $P_{\text{SW}}$ , equal to the pressure of the SN shock (see, e.g., Fields et al. 2008). In this case, the pressure from the SN has little effect on the Earth, but by pushing back the solar wind, the Earth is inside the SN remnant and now directly exposed to the SN cosmic-rays that would normally diffuse out over  $10^4$  yr (Fujita et al. 2010) in addition to an increased galactic cosmic-ray background. In-turn, these destroy  $O_3$  and  $N_2$  in the atmosphere, just as in the direct exposure case, in addition to increased radionuclide deposition (Melott & Thomas 2011). Using our fiducial SN values, we find:

$$R_{\text{kill}} = 10 \text{ pc} \left( \frac{E_{\text{SN}}}{10^{51} \text{ ergs}} \right)^{1/3} \left( \frac{2 \times 10^{-8} \text{ dyne cm}^{-2}}{P_{\text{SW}}} \right)^{1/3} \quad (4)$$

The fadeaway distance is the range at which the SN shock dissipates and slows to the sound speed of the ISM. Because of uncertainty in when SN dust decouples from the rest of the shock, the fadeaway distance

---

<sup>3</sup>Note, our kill distance does not include the case of a gamma-ray burst given their narrowly-beamed emission.

is not an absolute limitation like the kill distance, but can serve as a guide to the likelihood of a progenitor. Using the derivation from Draine (2011, Eq. 39.31), we find:

$$R_{\text{fade}} = 160 \text{ pc} \left( \frac{E_{\text{SN}}}{10^{51} \text{ ergs}} \right)^{0.32} \left( \frac{0.1 \text{ cm}^{-3}}{n_{\text{ISM}}} \right)^{0.37} \left( \frac{10 \text{ km s}^{-1}}{c_s} \right)^{2/5} \quad (5)$$

### 3.2. SAGB Expansion Profile and Constraints

In the case of SAGBs, we assume the dust is ejected radially and that the distance traveled by SAGB dust is determined only by a drag force,  $F_{\text{drag}}$  (magnetic forces will be considered later in this section as a constraint). Using the description in Draine & Salpeter (1979), the drag force due to only collisional forces (in cgs units) is:<sup>4</sup>

$$F_{\text{drag}} = 2\pi a^2 kT \left( \sum_j n_j [G_0(s_j)] \right) \quad (6)$$

with

$$G_0(s) \approx \frac{8s}{3\sqrt{\pi}} \left( 1 + \frac{9\pi}{64} s^2 \right)^{1/2}, \quad s_j \equiv (m_j v^2 / 2kT)^{1/2} \quad (7)$$

where  $j$  is the respective species in the ISM (we consider only ionized H; He and free electrons will be neglected),  $m_j$  is the particle mass of that respective species,  $k$  is the Boltzmann constant,  $T$  is the temperature of the ISM, and  $v$  is the velocity of the particle relative to the medium. For small  $v$  (i.e.,  $v_{\text{grain}} \lesssim 100 \text{ km s}^{-1}$ ) the first term in  $G_0$  will dominate, leaving  $G_0(s) \approx 8s/(3\sqrt{\pi})$ . Making these simplifications, we find:

$$F_{\text{drag}} = 2\pi a^2 kT n_{\text{ISM}} v_{\text{grain}} \left( \frac{8}{3\sqrt{\pi}} \right) \left( \frac{m_p}{2kT} \right)^{1/2} = m_{\text{grain}} \ddot{R}_{\text{SAGB}} \quad (8)$$

where  $R_{\text{SAGB}}$  is the distance the dust grain has traveled from the SAGB, and  $v_{\text{grain}} \equiv \dot{R}_{\text{SAGB}}$ . Integrating twice and setting  $R_{\text{SAGB}}$  equal to the traverse distance from the progenitor to Earth,  $D$ , gives the transit interval:

$$t_{\text{travel,SAGB}} = -\zeta_0 \left( \frac{a\rho_{\text{grain}}}{c_s \rho_{\text{ISM}}} \right) \ln \left( 1 - \frac{1}{\zeta_0} \frac{c_s \rho_{\text{ISM}}}{a\rho_{\text{grain}} v_{\text{grain},0}} \frac{D}{v_{\text{grain},0}} \right) \quad (9)$$

where  $\zeta_0$  is a dimensionless constant and of order unity for  $\gamma = 5/3$ ,  $c_s$  is the sound speed in the ISM, and  $v_{\text{grain},0}$  is the initial velocity of the dust grain when it leaves the SAGB.

We approximate the density profile for a SAGB signal by a uniform shell or “top-hat” shape (we will use “top-hat” profile to avoid confusion with the SN profile discussion). This corresponds to a uniform, steady wind. The top-hat pattern reaches its maximum density value at the leading edge of the signal, retains this value for the duration of the signal, and afterwards the density returns to zero. The SAGB phase is characterized by thermal-pulsing of the star’s envelope. Since the duration of each pulse ( $\Delta t_{\text{pulse}} \sim 1 \text{ yr}$ ) and interval between pulses ( $\Delta t_{\text{inter}} \sim 100 \text{ yr}$ ) are much shorter than the SAGB phase ( $\Delta t_{\text{SAGB}} \sim 100 \text{ kyr} \gg \Delta t_{\text{inter}} > \Delta t_{\text{pulse}}$ ) we assume that the amount of ejected material is approximately constant for the duration of the SAGB phase (see Siess 2010). Furthermore, we assume all parts of the signal experience the same forces from the SAGB to the Earth, so that the duration of the signal remains the same (i.e.,  $\Delta t_{\text{signal,SAGB}} = \Delta t_{\text{SAGB}} = 100 \text{ kyr}$ ).

---

<sup>4</sup>The Coulomb force can be large, however, it is not for our selected grain parameters, so we neglect Coulomb forces (see constraints for  $(\phi^2 \ln \Lambda)$  in Draine 2011, §26.1.1).



Because SAGB winds would not be as devastating to the Earth as a SN shock, we forego establishing an inner kill distance, but establish two outer distances: the drag stopping distance,  $R_{\text{drag}}$ , and the magnetic deflection distance,  $R_{\text{mag}}$ . The distance,  $R_{\text{drag}}$ , is the range of the SAGB dust grains’  $e$ -folding velocity, and the  $R_{\text{mag}}$  is the range at which deflection of the dust grain’s trajectory by the ISM’s magnetic field becomes significant. Using the derivations from Murray et al. (2004), we find:

$$R_{\text{drag}} = 93 \text{ kpc} \left( \frac{\rho_{\text{grain}}}{3.5 \text{ g cm}^{-3}} \right) \left( \frac{a}{0.2 \text{ }\mu\text{m}} \right) \left( \frac{0.005 \text{ cm}^{-3}}{n_{\text{ISM}}} \right) \left( \frac{10^6 \text{ K}}{T} \right)^{1/2} \left( \frac{v_{\text{grain},0}}{30 \text{ km s}^{-1}} \right) \quad (10)$$

$$R_{\text{mag}} = 0.02 \text{ pc} \left( \frac{\rho_{\text{grain}}}{3.5 \text{ g cm}^{-3}} \right) \left( \frac{0.5 \text{ V}}{\mathcal{V}} \right) \left( \frac{5 \text{ }\mu\text{G}}{B} \right) \left( \frac{v_{\text{grain},0}}{30 \text{ km s}^{-1}} \right) \left( \frac{a}{0.2 \text{ }\mu\text{m}} \right)^2 \quad (11)$$

The implications of these limits will be discussed in greater detail in §6.

### 3.3. The Radioactivity-based Distance to the Explosion

To estimate the distance,  $D$ , to the explosion, we wish to invert Equation (1). When the transit time (the time for the shock to travel from the source to Earth) is negligible ( $t_{\text{travel}} \ll \tau_i$ ), the procedure is straightforward, since the only distance dependence is the inverse square dilution of the ejecta, and so  $D \propto 1/\sqrt{\mathcal{F}_{\text{obs},i}}$ .<sup>5</sup> This has been assumed in work to date. However, if  $D$  is sufficiently large, then via Equation (2), the distance-dependent transit time can become important and must be included in solving Equation (1); we have done this in all of our results.

Another effect occurs when the radioisotope signal is sampled sufficiently finely to resolve the time history of the deposition signal. This occurs when the signal width (the time from the arrival of the signal’s leading edge to the departure of the signal’s trailing edge) is larger than the sampling time resolution ( $\Delta t_{\text{signal}} > \Delta t_{\text{res}}$ ). In this case, the total radioisotope signal, summed over all time bins, should be used in solving the distance via Equation (1); and as we show in §3.5 below, the width of  $\Delta t_{\text{signal}}$  for a SN probes independently the explosion distance. However, the available Knie et al. (2004) data has a time sampling of  $\Delta t_{\text{res}} \sim 880 \text{ kyr}$ , and shows no evidence for a signal that is extended in time. Thus we infer that the signal width  $\Delta t_{\text{signal}} \lesssim \Delta t_{\text{res}}$ , and indeed we find  $\Delta t_{\text{signal}} \lesssim 880 \text{ kyr}$  for most of our possible progenitors. In addition, when solving for distance using the Knie results, we assumed the signal arrived halfway through the sample. Therefore, half of the sampling width is used as a median value rather than assuming the signal arrives right as the sampling window begins or just before it ends.

### 3.4. Expected Behavior of Time-Resolved Signals

Although the time resolution of the deep-ocean  $^{60}\text{Fe}$  crust measurements in Knie et al. (2004) data preclude resolution of the time structure of the radioisotope deposition, measurements in sediments can achieve much better time resolution, and so it is of interest to explore the time dependence of the explosion signal. Such work was pioneered by Ammosov et al. (1991) in the context of the  $^{10}\text{Be}$  anomalies  $\sim 35$  and  $60 \text{ kyr}$  ago in Antarctic ice cores (Raisbeck et al. 1987).

---

<sup>5</sup>This “radioactivity distance” is analogous to the usual luminosity distance: the yield plays the role of luminosity, and radioisotope fluence the role of flux (Looney et al. 2006).

In developing a model for deposition, we examine a Sedov-Taylor profile for a SN shock (a similar examination could be done for the SAGB case if we had more detailed description of its signal width dependence), which implies an energy-conserving (adiabatic) evolution. This also means the shock will remain self-similar as it progresses and that the majority of the material is concentrated near the leading edge. Although the remnant density profile changes once the remnant transitions to the radiative/momentum-conserving phase, we have chosen to maintain the Sedov profile. We did this, firstly, because the profiles are similar in shape (the radiative profile is a thicker shell profile, see, e.g., Shu 1992, Fig. 17.4). Secondly, because the dust will decouple from the gas at some point, either when the shock meets back pressure from encountering the solar wind or at the transition from the adiabatic to the radiative phase when the shock loses its internal radiation pressure (Draine 2011). The exact nature of this decoupling and resulting profile would require detailed calculations that are beyond the scope of this paper.

We assume that the explosion ejecta are well-mixed within the swept-up matter, so that the ejecta density profile follows that of the blast itself. As described in Appendix B, we approximate the Sedov density profile as a “saw-tooth” that drops linearly from a maximum behind the shock radius  $R_{\text{SN}}$  to zero at an inner radius  $r_{\text{in}} = (1 - \epsilon)R_{\text{SN}}$ , with  $\epsilon \approx 1/6$ . We note that the leading edge of the blast from an event at distance  $D$  arrives at a time  $t_{\text{travel}}$  since the explosion which corresponds to geological time  $t_{\text{arr}}$ ; this is given by  $D = R_{\text{SN}}(t_{\text{arr}})$ , whereas the trailing edge of the shell arrives at time  $t_{\text{dep}}$  given by  $D = (1 - \epsilon)R_{\text{SN}}(t_{\text{dep}})$ . Thus we have  $t_{\text{dep}} = t_{\text{arr}}/(1 - \epsilon)^{5/2}$ .

With these assumptions we can model the global-averaged flux time profile,  $\mathbb{F}$ . For radioisotope  $i$ , we have:

$$\mathbb{F}_i(D, t) = \left(\frac{t}{t_{\text{arr}}}\right)^{-11/5} \left[\frac{(t/t_{\text{arr}})^{-2/5} - (t_{\text{dep}}/t_{\text{arr}})^{-2/5}}{1 - (t_{\text{dep}}/t_{\text{arr}})^{-2/5}}\right] \mathbb{F}_i(D, t_{\text{arr}}) \quad (12)$$

as shown in Appendix B; note that here all times are geological and thus increase towards the past.<sup>6</sup> This describes a cusp-shaped decline from an initial flux:

$$\mathbb{F}_i(D, t_{\text{arr}}) = \frac{2\mathcal{F}_1}{5t_{\text{arr}}} = \frac{3}{40\pi} \frac{\gamma + 1}{\gamma - 1} \frac{M_{\text{ej},i}/m_i}{D^2} \left(\frac{\xi_0^5 E_{\text{SN}}}{m_p n_{\text{ISM}} D^5}\right)^{1/2} \quad (13)$$

$$= 9.5 \times 10^5 \text{ atoms cm}^{-2} \text{ kyr}^{-1} \quad (14)$$

$$\times \left(\frac{0.1 \text{ cm}^{-3}}{n_{\text{ISM}}}\right)^{1/2} \left(\frac{E_{\text{SN}}}{10^{51} \text{ ergs}}\right)^{1/2} \left(\frac{M_{\text{ej},i}}{3 \times 10^{-5} M_{\odot}}\right) \left(\frac{60}{A_i}\right) \left(\frac{100 \text{ pc}}{D}\right)^{9/2}$$

where the numerical values are  $m_i = 60m_u$  and the yield is appropriate for  $^{60}\text{Fe}$ .

To test the profile in Equation (12), one can fit observed time-resolved data to this form, letting  $t_{\text{arr}}$  and  $t_{\text{dep}}$ , and  $\mathbb{F}_i(D, t_{\text{arr}})$  be free parameters. For the Sedov profile, the time endpoints should obey  $t_{\text{dep}} = t_{\text{arr}}/(1 - \epsilon)^{5/2}$ , which provides a consistency check for the Sedov (adiabatic) approximation. Moreover, as we show in §3.5, the interval  $t_{\text{dep}} - t_{\text{arr}}$  provides an independent measure of the explosion distance.

If the radioisotope abundance is sampled over a time interval  $[t_1, t_2]$ , then the fluence (without radioactive decays) will be the integral of the surface flux over this interval:  $\mathcal{F}_i(t_1, t_2) = \int_{t_1}^{t_2} \mathbb{F}_i(t) dt$ , where we have suppressed the dependence on time-independent parameters such as distance. If the observed time resolution  $\Delta t_{\text{res}}$  is small compared to  $t_{\text{arr}}$  and  $t_{\text{dep}}$ , then the fluence profile  $\mathcal{F}_i(t - \Delta t_{\text{res}}/2, t + \Delta t_{\text{res}}/2) \approx \mathbb{F}_i(t) \Delta t_{\text{res}}$  will recover the flux history.

---

<sup>6</sup>In Equation (2) time increases towards the future, but note that elsewhere, unless explicitly stated, times are used in the geological sense, and thus increase towards the past.

So far we have calculated the observed fluence without the effect of decay. Since all the atoms were created at the same time, the observed fluence is reduced by a factor  $e^{-(t_{\text{arr}}+t_{\text{travel}})/\tau_i}$ . The effects of uptake (§4.1) and dust depletion (§4.2) introduce further factors of  $U_i$  and  $f_i$ . We thus arrive at the observed fluence:

$$\mathcal{F}_{\text{obs},i}(t_1, t_2) = U_i f_i e^{-(t_{\text{arr}}+t_{\text{travel}})/\tau_i} \int_{t_1}^{t_2} \mathbb{F}_i(t) dt . \quad (15)$$

One can show that the total integrated fluence  $\mathcal{F}_{\text{obs},i}(t_{\text{arr}}, t_{\text{dep}})$  takes precisely the value in Equation (1). This reflects the number conservation (aside from decays) of the atoms in the SN ejecta. This also implies that, in a time-resolved measurement, the total fluence is conserved, which means that the area under a fluence vs. time curve will be constant for fixed explosion parameters. This implies that fluence measurements of  $^{60}\text{Fe}/\text{Fe}$  will show lower values when measured over fewer bins, and finer sampling will show higher fluence over more bins (see Figure 1).

### 3.5. A Resolved Signal Timescale Probes the Distance to the Explosion

A time-resolved signal not only encodes information about the shape of the blast density profile, but also about the distance. The relation  $D = (1 - \epsilon)R_{\text{SN}}(t_{\text{dep}})$  also allows us to write  $t_{\text{dep}} = t_{\text{arr}}/(1 - \epsilon)^{5/2}$  and thus that:

$$\Delta t_{\text{signal}} = t_{\text{dep}} - t_{\text{arr}} \equiv \alpha t_{\text{arr}} \quad (16)$$

where we define a dimensionless parameter,  $\alpha$ , that relates the signal width in terms of the arrival time. For our profile,  $\alpha = (1 - \epsilon)^{-5/2} - 1 \approx 0.577$ . We see that the radioisotope width grows in proportion to the blast transit time to Earth,  $t_{\text{travel}}$ , which itself depends on distance. Thus a measurement of  $\Delta t_{\text{signal}}$  from a time resolved radioisotope signal gives an measure of the explosion distance. Within this Sedov model,  $D = R_{\text{SN}}(t_{\text{arr}})$ , and so we can solve for the distance based on “blast timing:”

$$D = \xi_0 \left( \frac{E_{\text{SN}} \Delta t_{\text{signal}}^2}{\alpha^2 \rho} \right)^{1/5} \quad (17)$$

$$= 65 \text{ pc} \left( \frac{\Delta t_{\text{signal}}}{100 \text{ kyr}} \right)^{2/5} \left( \frac{E_{\text{SN}}}{10^{51} \text{ ergs}} \right)^{1/5} \left( \frac{0.1 \text{ cm}^{-3}}{n_{\text{ISM}}} \right)^{1/5} \quad (18)$$

This distance measure is independent of the “radioactivity distance” and its associated uncertainties, notably due to uptake, dust fraction, and radioisotope yields. Moreover, as characteristic for Sedov blast waves, the blast-timing distance in Equation (17) scales as small powers of the timescale, as well as the energy and density. This will weaken the uncertainties in distance estimate.

Having two independent distance estimates allows a consistency check for the model. Alternatively, if we adopt one of the distance estimates as the correct value, we can deduce the parameters in the other. For example, adopting the blast-timing distance we can use the observed fluence and solve for the product of radioisotope yield, uptake, and dust fraction:  $M_{\text{ej},i} U_i f_i \propto D^2 \mathcal{F}_{\text{obs},i}$ . Given a geophysical estimate of uptake, this allows for a measure of the yield and thus a direct probe of the nucleosynthesis output and thus the nature of the explosion (see Figure 1 for examples).

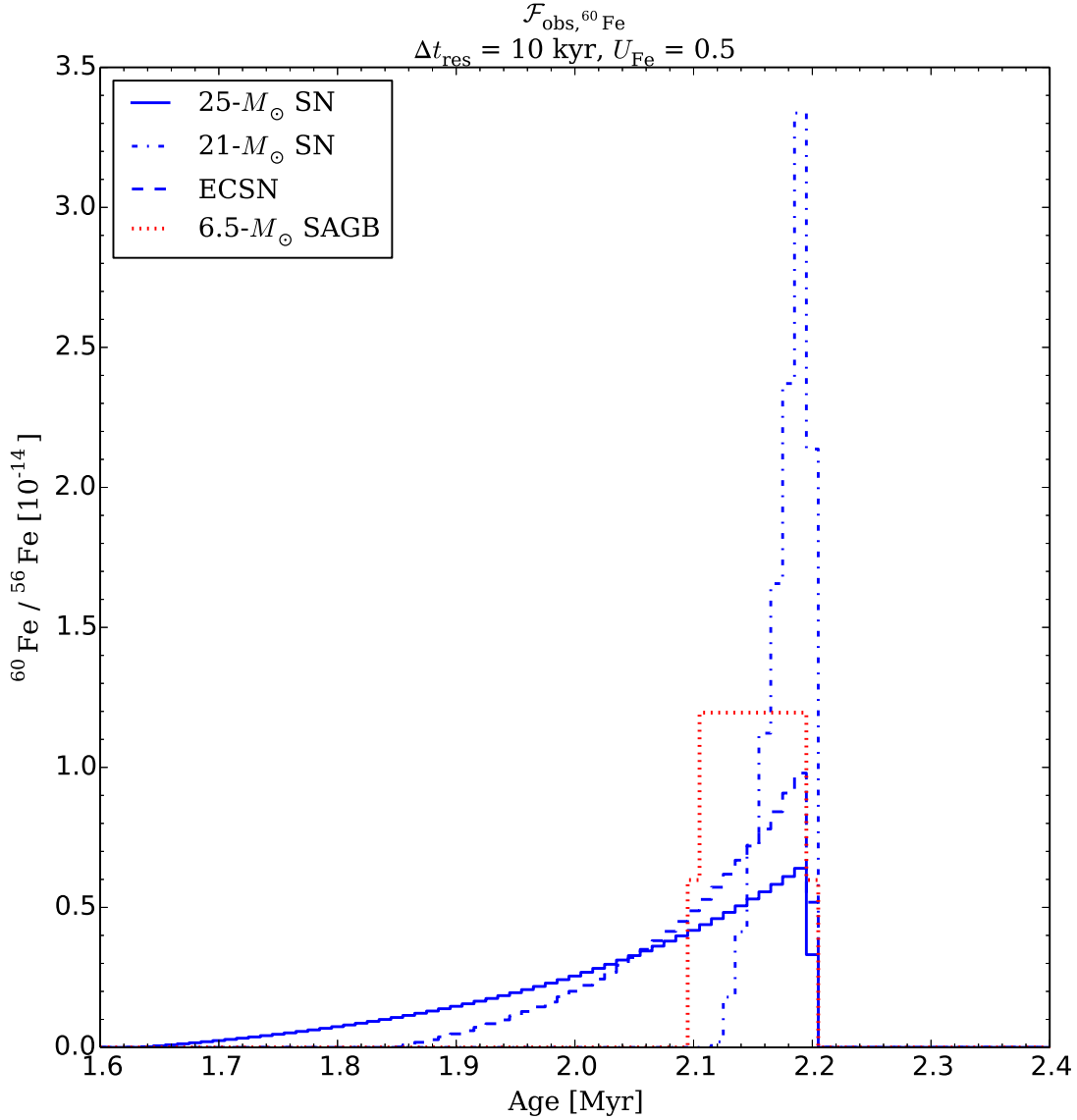


Fig. 1.— Sample time-resolved calculations of the observed fluence,  $\mathcal{F}_{\text{obs}, {}^{60}\text{Fe}}$ , for three SNe and a SAGB. Each progenitor is at a different distance:  $25-M_{\odot}$  SN at 130 pc,  $21-M_{\odot}$  SN at 59 pc, ECSN at 67 pc, and  $6.5-M_{\odot}$  SAGB at 79 pc. Of note, each of these progenitors would produce the same measured  ${}^{60}\text{Fe}$  signal by Knie et al. (2004); Fitoussi et al. (2008), but with a finer time-resolution (10 kyr in this case), the shape of the signal is readily discernible. Also note that since the plots produce the same observed fluence, the areas under the curves are the same.

## 4. Deposit Factors

The delivery of astrophysical debris to the Solar System and its incorporation into geological and lunar samples is clearly complex. In this section we consider several factors we are aware of that can have a substantial influence on the observed signals.

### 4.1. Uptake

Uptake in the Fe-Mn crust involves a complex chemical process that incorporates material into the crust with a low accumulation rate  $\sim 2 \text{ mm Myr}^{-1}$ . Usual deep-ocean sediments, on the other hand, do not make such a geochemical selection, and have greater accumulation rates  $\sim 3 - 4 \text{ mm kyr}^{-1}$  (Feige et al. 2012). The Fe uptake factor was calculated by Knie et al. (2004) using the relative concentrations of Fe and Mn in water and the Fe-Mn crust and the uptake of Mn (4%), leading to an estimate for the Fe uptake,  $U_{\text{Fe}} = 0.6\%$ . However, recent studies have suggested that  $U_{\text{Fe}} = 0.5 - 1$  (Bishop & Egli 2011; Feige et al. 2012). Using the smaller estimate of  $U_{\text{Fe}}$ , Knie et al. (2004) calculated a SN distance of  $D \approx 40 \text{ pc}$ ; a reasonable distance considering the Local Bubble is  $\sim 200 \text{ pc}$  in diameter in the Galactic plane extending 600 pc perpendicular to the plane (Fuchs et al. 2006) and superbubbles in the Large Magellanic Cloud (LMC) are typically  $\sim 100 - 200 \text{ pc}$  in diameter (for a single round of star formation, Chu 2008). Changing the uptake factor has the immediate effect of changing the implied distance to the explosion. This can be roughly understood if we ignore the effect of the debris decays in transit, in which case the signal follows the inverse square law and we have  $D \propto \sqrt{U_i/\mathcal{F}_{\text{obs},i}}$ . The effect of decays en route softens this dependence somewhat.

If  $U_{\text{Fe}}$  is an order of magnitude larger, the implied distance increases by a factor  $\gtrsim 2$ . With a Fe-Mn crust uptake factor of  $U_{\text{Fe}} = 0.5 - 1$ , the implied distances are around  $D \sim 200 \text{ pc}$ . This seems an unlikely distance, given that the Solar System is roughly in the center of the Local Bubble (see Berghöfer & Breitschwerdt 2002, Fig. 2), and a SN would have had to occur outside the Local Bubble in order to produce the signal (assuming the progenitor is in the Galactic plane).

However, implicit in the Knie et al. (2004) calculation is the assumption that the dust fraction,  $f_{\text{Fe}} = 1$ . As we will show in §4.2, this is most likely not the case, and the combination of a higher uptake value (we chose  $U_{\text{Fe}} = U_{\text{Al}} = 0.5$ ) with a smaller dust fraction ( $f_i \ll 1$ ) can still yield reasonable progenitor distances.

### 4.2. Dust Condensation

It was shown in Fields et al. (2008), that for a SN further than  $D \sim 10 \text{ pc}$ , the solar wind would keep the SN blast plasma outside of 1 AU, and thus the Earth will not find itself inside gas-phase SN debris. However, refractory SN ejecta will be condensed into dust grains. As discussed in Athanassiadou & Fields (2011), we expect these grains to be entrained in the SN blast as it reaches the heliosphere, but then decouple at the SN-solar wind shock and move essentially ballistically through the inner solar system. Once the dust decouples from the gas in the shock, it can travel great distances. At this point, both SNe and SAGBs behave the same, as they are subject to the same drag stopping distance,  $R_{\text{drag}}$  discussed in §3.2. This is more than sufficient to reach the Earth in spite of the solar wind, and indeed should carry dust grains beyond the SN remnant when it finally comes to rest. Thus, for the  $D > 10 \text{ pc}$  events of interest, the amount of any radioisotope  $i$  that comes to Earth will be proportional to the fraction,  $f_i$ , of the isotope that reaches Earth via dust, as seen in Equations (1) and (15).

Determining  $f_i$  requires examining a number of factors (the results are summarized in Table 2):

- 1) How much of the isotope condenses into dust at departure from source?
- 2) How much of that dust survives the interstellar journey from the source to the Solar System?
- 3) How much of the remaining dust can filter through the heliopause and enter the Solar System?
- 4) How much of the filtered dust can overcome the solar wind/radiation pressure and reach the Earth’s orbit?

In order to determine the isotope fraction that condenses into dust, we use recent observations of SN 1987A. *Herschel* observations in the far infrared and sub-millimeter wavelengths were modeled in Matsuura et al. (2011) with different elemental abundances and dust compositions. In both models studied, the synthesized Fe mass was nearly identical to the Fe condensed into dust. This suggests that after less than 30 yrs (much less time than required to travel to a nearby solar system), practically all of the iron from the SN is in the form of dust. Furthermore, when comparing condensation temperatures (Spitzer & Jenkins 1975), one finds that  $T_{C,Al} = 1800 \text{ K} > T_{C,Fe} = 1500 \text{ K}$ , suggesting Al would condense into dust at the same time as Fe, if not sooner. Based on this reasoning, we assume 100% of Al and Fe condenses into dust for both SNe and SAGBs.

While refractory elements seem to condense rapidly after ejection, only the dust that survives transport to the Solar System will reach the Earth. Dust leaving from SAGBs will be subject to shocks from neighboring star systems as well as sputtering from radiation and collisions with other dust grains. However, for the purposes of this paper, we will assume these effects are negligible compared to other filtering effects examined. Therefore, we will assume all of the dust from SAGBs are able to pass from the SAGB to the Solar System (a more in-depth discussion of interstellar effects on dust grains is discussed in Murray et al. 2004).

Conversely, SN remnants are likely to be much harsher environments for dust, leading to predictions of very small survival probabilities for some dust species and thus for some radioisotopes. Dust formed from ejecta in a newborn SN remnant will encounter a reverse shock as the remnant transitions from the free expansion to the Sedov/adiabatic phase. The reverse shock propagates from the outer edge of the remnant back to the source and is generally stronger than the interface between the outer edge of the remnant and general ISM. The reverse shock causes large-scale sputtering/destruction of grains resulting in gas phase emission from previously refractory elements (e.g., see emission from Cassiopeia A, Rho et al. 2008). Silvia et al. (2010, 2012) studied this interaction and found grains  $\lesssim 0.1 \mu\text{m}$  to be most affected;  $\sim 1\%$  of  $\text{Al}_2\text{O}_3$  (corundum),  $\sim 50\%$  of FeS (troilite), and  $\sim 100\%$  of Fe (metallic iron) previously condensed into dust survives.

Once the dust reaches the Solar System, it must pass through the heliosphere to reach the Earth. Linde & Gombosi (2000) suggested a cut-off grain size of  $0.1 - 0.2 \mu\text{m}$  for filtering by the heliosphere for grains with speeds of  $26 \text{ km s}^{-1}$  corresponding to the Sun’s motion through the local ISM. This filtering is less severe for faster dust grains (Athanasiadou & Fields 2011), but for our larger SN distances we find slower speeds in Table 3. Since magnetohydrodynamic simulations by Slavin et al. (2010) showed penetration but strong deflection of  $0.1 \mu\text{m}$  grains, we chose a minimum grain size of  $0.2 \mu\text{m}$  for entering the Solar System. For SN dust, this cut-off means that negligible amounts of  $\text{Al}_2\text{O}_3$  and FeS grains will enter the Solar System, while  $\sim 10\%$  of Fe grains will be large enough to pass through. For SAGB dust, we assume the Fe is in elemental Fe and silicate grains (distributed according to Pollack et al. (1994) with FeS assumed to be Fe); Al will be in  $\text{Al}_2\text{O}_3$ , but with a larger grain size (Hoppe & Zinner 2000). The Fe size distribution is assumed to be the same as for SN (Sterken et al. 2013), and silicate grains are assumed to follow the Mathis et al.

Table 2: Summary of Relevant Dust Filtering Processes

Resulting Dust Fraction	Repository Material	Density	Elemental fraction in material	Fraction condensed into dust	Fraction surviving interstellar passage	Fraction passing into heliosphere	Fraction reaching Earth's orbit
$f_{\text{Fe,SN}} \approx 0.01$	Fe	7.9	$0.1^a$	$1^c$	$1^a$	$0.1^{a,d}$	$1^g$
	FeS	4.8	$0.9^a$	$1^c$	$0.5^a$	$0^{a,d}$	$1^g$
$f_{\text{Fe,SAGB}} \approx 0.2$	Fe	7.9	$0.48^b$	$1^c$	1	$0.1^{a,d}$	$1^g$
	[Fe, Mg] <sub>2</sub> SiO <sub>4</sub>	3.5	$0.43^b$	$1^c$	1	$0.25^{d,e}$	$1^g$
	[Fe, Mg]SiO <sub>3</sub>	3.5	$0.09^b$	$1^c$	1	$0.25^{d,e}$	$1^g$
$f_{\text{Al,SN}} \approx 0$	Al <sub>2</sub> O <sub>3</sub>	4	$1^a$	$1^c$	$0.01^a$	$0^{a,d}$	$1^g$
$f_{\text{Al,SAGB}} \approx 1$	Al <sub>2</sub> O <sub>3</sub>	4	$1^a$	$1^c$	1	$1^{d,f}$	$1^g$

Density is given in  $\text{g cm}^{-3}$ .

Mass fractions from each filter process are determined using the relative size number distributions,  $N(a)$ , given in Silvia et al. (2010) and Mathis et al. (1977), multiplying by volume,  $V(a)$ , and density,  $\rho$ , and integrating over the relevant radii [ $a_{\text{max}}$ ,  $a_{\text{min}}$ ]. This method is described in Mathis et al. (1977):  $m = \int_{a_{\text{min}}}^{a_{\text{max}}} \rho N(a) V(a) da$ .

<sup>a</sup> - Silvia et al. (2010)

<sup>b</sup> - Pollack et al. (1994), Table 1B. Given the temperature of the Local Bubble ( $T > 1000 \text{ K}$ ), it is assumed all FeS has been converted to Fe.

<sup>c</sup> - Matsuura et al. (2011) and Spitzer & Jenkins (1975)

<sup>d</sup> - Slavin et al. (2010)

<sup>e</sup> - Mathis et al. (1977)

<sup>f</sup> - Hoppe & Zinner (2000)

<sup>g</sup> - Burns et al. (1979) and Gustafson (1994)

(1977) distribution ( $dN/da \propto a^{-3.5}$ ) ranging from 0.5-350 nm (Weingartner & Draine 2001). This means  $\sim 10\%$  of Fe,  $\sim 25\%$  of silicates, and  $\sim 100\%$  of Al from SAGBs will enter the Solar System.

Lastly, the dust grain must overcome the Sun’s radiation pressure once it is in the Solar System. For this, we consider the parameter  $\beta$  (Burns et al. 1979) that characterizes the ratio of the Sun’s radiation force,  $F_r$ , to the gravitational force,  $F_g$ :

$$\beta \equiv \frac{F_r}{F_g} = C_r Q_{\text{pr}} \frac{3}{4a\rho_{\text{grain}}} \quad (19)$$

where  $C_r$  is  $7.6 \times 10^{-5} \text{ g cm}^{-2}$  and  $Q_{\text{pr}}$  is the efficiency of the radiation on the grain (we will assume  $Q_{\text{pr}} \sim 1$  for the size of grains we are interested in, Gustafson 1994). From Sterken et al. (2013), only dust grains with  $\beta \lesssim 1.3$  will reach Earth’s orbit; based on the densities of the minerals considered, if the grain can enter the Solar System, it will be able to reach Earth’s orbit.

Combining each of these factors, we find for SNe:  $f_{\text{Fe,SN}} \approx 0.01$  and  $f_{\text{Al,SN}}$  is negligible. For SAGBs:  $f_{\text{Fe,SAGB}} \approx 0.2$  and  $f_{\text{Al,SAGB}} \approx 1$ . In spite of the number of considerations in determining these quantities, there are still others that could be included, namely a velocity dependence on the filtering by the heliopause. We would expect dust grains with a sufficiently high velocity (i.e.,  $v_{\text{grain}} > v_{\text{esc},\odot}$ ) to ignore size filtering limitations, but including these effects will be left for a future work.

## 5. Live Radioisotope Data

### 5.1. Terrestrial Measurements of $^{60}\text{Fe}$

The primary data value for our analysis is the decay-corrected  $^{60}\text{Fe}$  fluence measured by Knie et al. (2004) in a deep-ocean Fe-Mn crust. They found an isotopic ratio of  $^{60}\text{Fe}/\text{Fe} = 1.9 \times 10^{-15}$  within the crust; this corresponds to a decay-corrected fluence of  $\mathcal{F}_{\text{arr},60} = (2.9 \pm 1.0) \times 10^6 \text{ atoms cm}^{-2}$ . This may be used to determine the distance from the progenitor. At the time of the original measurements, the half-life of  $^{60}\text{Fe}$  was estimated to be 1.49 Myr and that of  $^{10}\text{Be}$  was estimated to be 1.51 Myr, resulting in an arrival time,  $t_{\text{arr}} = 2.8 \text{ Myr ago}$ . Since then, the half-lives have been refined: current best estimates being  $\tau_{1/2, ^{60}\text{Fe}} = 2.62 \text{ Myr}$  and  $\tau_{1/2, ^{10}\text{Be}} = 1.387 \text{ Myr}$ , and this places the signal arrival at 2.2 Myr ago. To update the Knie  $^{60}\text{Fe}$  fluence, we use ratios to convert the previous results to the updated values that are similar in method to those employed by Bishop & Egli (2011) and Feige et al. (2012):  $\mathcal{F}_{60,\text{update}}/\mathcal{F}_{60,\text{previous}} = e^{-t_{60,\text{update}}/\tau_{60,\text{update}}} / e^{-t_{60,\text{previous}}/\tau_{60,\text{previous}}}$ , which gives the following updated, decay-corrected fluence in the crust:

$$\mathcal{F}_{\text{arr},60(\text{updated})} = (1.41 \pm 0.49) \times 10^6 \text{ atoms cm}^{-2} \quad (20)$$

The  $^{60}\text{Fe}$  measurement in the crust has been verified by Fitoussi et al. (2008), but within this same work, no comparable  $^{60}\text{Fe}$  signal was detected in a sea sediment sample. Fitoussi et al. (2008) suggested several reasons for the non-detection in the sediment, including differences in uptake and divergences in the sediment from the global background. In addition, we note that the fluence calculation assumes an even distribution of dust over the Earth’s surface. However, the Earth’s wind patterns are not uniform, nor is Earth’s precessional axis necessarily orthogonal to the progenitor’s position. Consider, for example, a spherical dust grain of radius  $0.2 \mu\text{m}$  falling at terminal velocity ( $\sim 0.1 \text{ m s}^{-1}$ ) through a 1500 m-thick jet stream flowing horizontally at  $100 \text{ km hr}^{-1}$  with a density of  $4 \times 10^{-4} \text{ g cm}^{-3}$  (the assumption of falling at terminal velocity should be valid as the Earth’s atmosphere will have dissipated most of the dust grain’s remaining interstellar kinetic energy). As the dust grain falls, the pressure from the jet stream will quickly



accelerate the grain horizontally to the same velocity and push the grain  $\sim 300$  km before it falls out of the jet stream. In view of the non-uniformity of the jet stream’s flow as well as other terrestrial winds, anisotropies in the observed fluences are expected. Furthermore, one should also consider the source’s orientation to the Earth’s precessional axis; the Fe-Mn crust used by Knie et al. (2004) is from  $9^{\circ}18'$  N,  $146^{\circ}03'$  W ( $\sim 1,000$  mi/1,600 km SE of Hawaii), and the sediment used by Fitoussi et al. (2008) is from  $66^{\circ}56.5'$  N,  $6^{\circ}27.0'$  W ( $\sim 250$  mi/400 km NW of Iceland). The crust sample’s location relative to the equator would make it more likely to receive a signal over a range of arrival angles while the northern hemisphere could be partially shielded from a more southerly progenitor. Rather than the Fe-Mn crust signal being due to a misinterpretation of the global background, the absence of a sediment signal could be due to the geometry of the source’s position. If this is the case, a sediment sample from the southern hemisphere (e.g., ELT49-53,  $38^{\circ}58.7'$  S,  $103^{\circ}43.1'$  E and ELT45-21,  $37^{\circ}51.6'$  S,  $100^{\circ}01.7'$  E used by Feige et al. (2013)) should have an  $^{60}\text{Fe}$  signal.

## 5.2. Lunar Measurements of $^{60}\text{Fe}$

In addition to sea sediment and Fe-Mn crusts, lunar surface (regolith) samples can also be used to search for a nearby progenitor signal. The lunar surface is not affected by wind or water erosion, but, as pointed out by Feige et al. (2013), the sedimentation rate is low (precluding the possibility of time-resolved measurements) and regular impacts by a range of impactors (Langevin & Arnold 1977), continually churn up the regolith, mixing different levels. Lunar samples would be better suited to providing a “first hint” of a signature (Feige et al. 2013). Apollo core samples were analyzed by Cook et al. (2009), Fimiani et al. (2012), and Fimiani et al. (2014); in particular, these authors found both the Apollo 12 sample 12025 and Apollo 15 sample 15008 to have an  $^{60}\text{Fe}$  signal above the background. Nishiizumi et al. (1979) and Nishiizumi et al. (1990) found that the Apollo 12 and 15 cores, respectively, showed little to no large-scale mixing just prior to, during, and/or since the potential arrival of the signal, meaning no large impactor could have ejected part of the regolith thus diluting the signal. However, as we show in the next section, another issue arises with the dust’s arrival at the Moon’s surface that can dilute the signature.

## 5.3. Lunar Regolith and Dust Grains: Vaporization

As noted above, there are putative detections of a non-meteoritic  $^{60}\text{Fe}$  lunar anomaly, which seem to verify the presence of the deep-ocean signal; an amazing confirmation. However, having argued that the  $^{60}\text{Fe}$  will arrive in the form of high-velocity dust grains, we now consider the implications for the deposition onto the lunar surface.

Cintala (1992) made a detailed study of impacts on the lunar regolith and found semi-empirical fits to the volume of vapor produced as a function of impactor size and velocity and of the target composition. It was found that impactor velocity is the dominant factor and that, for  $v_{\text{grain}} > 100$  km s $^{-1}$ , the volume of target material that is vaporized is  $\sim 10 - 100$  times the volume of the impactor itself. More recently, Cremonese et al. (2013) showed that micrometeor impacts can be a non-negligible source of the lunar vapor atmosphere. They use the Cintala (1992) model and find that the contribution may be 8% of the photo-stimulated desorption at the subsolar point, becoming similar in the dawn and dusk regions and dominant on the night side. Moreover, Collette et al. (2014) did laboratory experiments to simulate micrometeorite impacts, studying the neutral gas created as a result. They find that the number of neutrals produced per

unit impactor mass scales as  $\sim v_{\text{grain}}^{2.4}$ , and they conclude that complete vaporization is expected for speeds exceeding  $20 \text{ km s}^{-1}$ .

With these results in mind, we now consider the conditions surrounding the arrival of the dust signal in question at the lunar surface. After entering the Solar System, the dust grains continue to the Earth/Moon at essentially the same speed. However, whereas the Earth’s atmosphere slows the arriving dust grains prior to reaching the surface, the Moon’s tenuous atmosphere has practically no influence, and the dust grains’ velocities are unchanged before arrival at the lunar surface. The dust grains are estimated to be  $\sim 0.2 \mu\text{m}$  in size, and moving at  $\sim 20 - 100 \text{ km s}^{-1}$  depending on the progenitor’s distance. Thus the grains behave as “micrometeorites” moving at very high speeds similar to those examined above.

Consider a silicate dust grain ( $\rho_{\text{grain}} \sim 3.5 \text{ g cm}^{-3}$ ) impacting the lunar surface ( $\rho_{\text{regolith}} \sim 1.6 \text{ g cm}^{-3}$ ) at  $v_{\text{grain}} \sim 20 \text{ km s}^{-1}$ . The grain arrives with kinetic energy  $E_{\text{grain}} = m_{\text{grain}}v_{\text{grain}}^2/2 \sim 0.23 \text{ ergs}$ , where  $m = 4\pi\rho_{\text{grain}}a^3/3$  is the mass of a spherical grain of radius  $a$ . The dust grain will penetrate the regolith to a depth comparable to its diameter and will vaporize some of the surrounding material; we will assume  $V_{\text{vapor}} = 10V_{\text{grain}} \Rightarrow m_{\text{vapor}} \approx 4.6m_{\text{grain}}$ . Given the grain’s high speed and shallow penetration, the vaporization will happen quickly (i.e., very little expansion occurs before the entire mass is vaporized). Moreover, since the initial density of the vaporized regolith is much greater than the density of the Moon’s atmosphere, the gas will behave as if it is expanding isentropically into a vacuum. The grain’s kinetic energy will go into vaporizing the grain and regolith and into the thermal and kinetic energy of the resulting gas. To determine the vaporization energy, the standard enthalpy of formation for the lunar regolith is  $\sim 1.5 \times 10^{11} \text{ ergs/g} = (3.9 \text{ km s}^{-1})^2$ . This is an approximate value for both of the lunar regolith’s main constituents, silica,  $\text{SiO}_2$ , and aluminum oxide,  $\text{Al}_2\text{O}_3$ , (Nava & Philpotts 1973), and includes both the vaporization and dissociation energies for the molecules. Therefore, the total energy consumed in vaporization is 0.1 ergs, leaving 0.13 ergs for the thermal and kinetic energy,  $E_{\text{vapor}}$ , of the gas.

As the gas expands, the thermal portion vanishes asymptotically, with all the energy becoming kinetic. Thus, after this cooling, the asymptotic expansion speed of the vaporized material is:

$$v_{\infty} = \sqrt{\frac{2E_{\text{vapor}}}{m_{\text{vapor}} + m_{\text{grain}}}} \approx 6 \text{ km s}^{-1} \quad (21)$$

[For further discussion, see Zel’dovich & Raizer (1967, p. 101-104, 844-846)].

The vapor speed is much larger than the lunar escape velocity,  $v_{\text{esc, Moon}} = 2.4 \text{ km s}^{-1}$ . This suggests that much of the vaporized material, including the dust impactor with its  $^{60}\text{Fe}$  material, would escape from the Moon. This would imply that the Moon has an uptake factor  $U_{\text{Moon}} \ll 1$ . Thus, we should not be surprised that the lunar results for  $^{60}\text{Fe}$  are lower than expected naively from the terrestrial Fe-Mn crust results. While lunar samples confirm the signal found in the Fe-Mn crust, they are less suitable for determining the fluence given the difficulties in determining  $U_{\text{Moon}}$ .

#### 5.4. $^{244}\text{Pu}$ Measurements

Several searches for live  $^{244}\text{Pu}$  have been performed, beginning with Wallner et al. (2000) looking at Fe-Mn nodules. Studies of top layer sea sediment by Paul et al. (2001), Paul et al. (2003), and Paul et al. (2007) have shown there is a very low background in  $^{244}\text{Pu}$ , making  $^{244}\text{Pu}$  an excellent candidate to confirm an  $^{60}\text{Fe}$  signal from an extra-solar source (presumably from a CCSN). Wallner et al. (2000, 2004) reported the detection of a single  $^{244}\text{Pu}$  atom in the same Fe-Mn crust sample used by Knie et al. (1999) and Knie et al.

(2004) covering the entire time interval of 1 – 14 Myr. Separately, Raisbeck et al. (2007) looked in sea sediment for a  $^{244}\text{Pu}$  signal, but did not find any evidence for a signal. It should be noted, however, that the Raisbeck study was using the previous arrival time (2.8 Myr ago) for his search. The samples were dated using magnetic polarization analysis and did not cover a large enough time interval to include the appropriate dating interval using the new value for the  $^{10}\text{Be}$  lifetime (Meynadier et al. 1994).

### 5.5. $^{26}\text{Al}$ Measurements

Feige et al. (2013) reported on searches for  $^{10}\text{Be}$  and  $^{26}\text{Al}$  using  $\sim 3$  kyr time intervals in samples from sea sediments ELT 49-53 and ELT 45-21. In the case of  $^{26}\text{Al}$ , the measurements showed only variations consistent with fluctuations around the background level, and found no evidence for an extra-solar signal. The paper also reported that  $^{53}\text{Mn}$  measurements are planned.

## 6. Results

In Figure 2 we compare our model predictions with the  $^{60}\text{Fe}$  data of Knie et al. (2004) and Fitoussi et al. (2008), showing that the model matches the results within the uncertainties for a SN or SAGB occurring 2.2 Myr ago. We note that the sampling was continuous through the entire data range, and straddled the signal arrival. In addition, the value for the 880-kyr time resolution was less than the 440-kyr sample, as expected due to the additional stable Fe in the wider sample.

Using the decay-corrected Knie et al. (2004) fluence of  $^{60}\text{Fe}$  (§5.1), and  $^{60}\text{Fe}$  yields from various source candidates (§2), we have solved Equation (1) for the distance to the source. Distances and other parameters for some of the possible sources appear in Table 3 and Figure 3. We see that, for sources at distances  $\sim 100$  pc that are typical of our subsequent estimated distances, the en route time and the signal width are  $\mathcal{O}(\text{Myr})$ , so it is possible that the signal could be time-resolved in future measurements, and thus it is of interest to model the signal shape.

### 6.1. Core-Collapse and Electron-Capture Supernovae

Figure 3 shows the calculated distances for our examined CCSNe and ECSN; they range from  $\sim 60 - 130$  pc. All CCSNe from our set lie outside of the kill distance and within the fadeaway distance for both their average fluence values and errors. Similarly, the ECSN lies outside the kill distance and within the fadeaway distance (the ECSN kill and fadeaway distances are shorter due to its lower explosive energy). The ECSN upper error is outside the fadeaway distance, but because SN dust can still travel great distances after decoupling, this is not an absolute limitation. Based on these distances, either a CCSN or an ECSN could have produced the measured  $^{60}\text{Fe}$  signal.

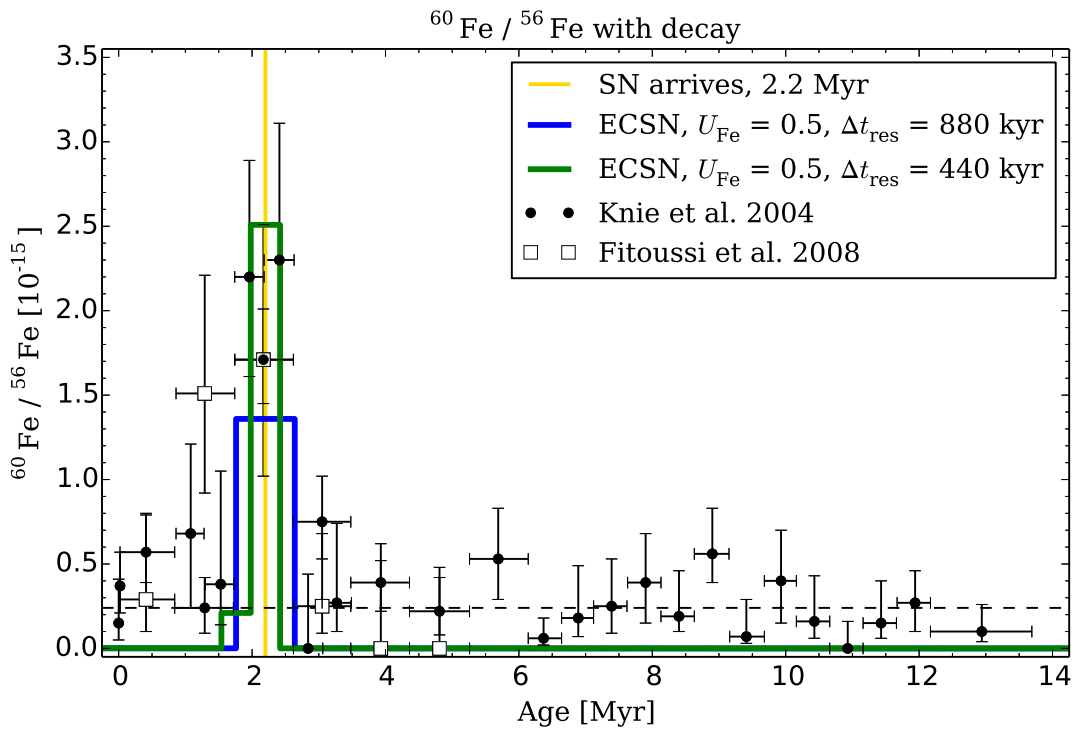


Fig. 2.— Evidence from Knie et al. (2004) and Fitoussi et al. (2008) for an anomalous peak in the  $^{60}\text{Fe}$  isotope fraction  $\sim 2.2$  Myr ago, compared with simulations of a possible signal from a SN explosion. We plot the results using ECSN yields; other progenitors yield similar results.

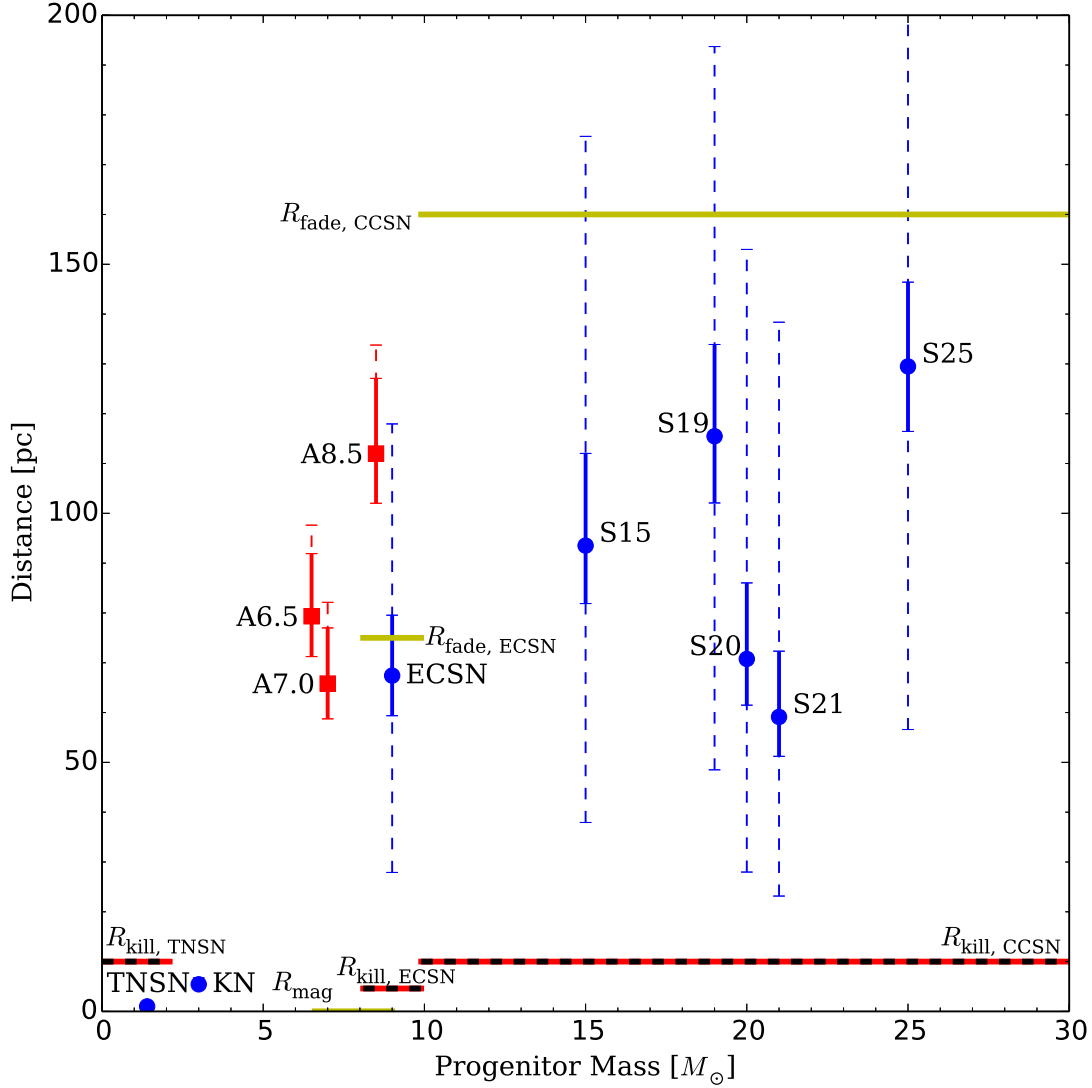


Fig. 3.— Estimated distances for possible progenitors, for  $U_{\text{Fe}} = 0.5$ . SN candidates are circles and SAGB candidates are squares. The solid error bars represent uncertainty in the fluence measurement (Knie et al. 2004). The dashed error bars represent additional uncertainty in  $^{60}\text{Fe}$  yields due to nuclear reaction rates in SNe (Tur et al. 2010) and a delayed super-wind phase in SAGBs (Doherty et al. 2013). Of particular note are the TNSN/Type Ia SN and the KN/NS-NS merger models, which are too close to have produced the detected  $^{60}\text{Fe}$  signal.

Table 3: Predicted Parameters for Possible  $^{60}\text{Fe}$  Signal Sources

Progenitor	Distance to Source, $D$ , pc	Time en route, $t_{\text{travel}}$ , Myr	Signal width, $\Delta t_{\text{signal}}$ , kyr	Arrival speed, $v_{\text{arr}}$ , km s $^{-1}$
6.5- $M_{\odot}$ SAGB	$79_{-8}^{+13}$	2.8	100	25
7.0- $M_{\odot}$ SAGB	$66_{-7}^{+11}$	2.3	100	26
7.5- $M_{\odot}$ SAGB	$73_{-8}^{+12}$	2.6	100	25
8.0- $M_{\odot}$ SAGB	$97_{-9}^{+14}$	3.5	100	24
8.5- $M_{\odot}$ SAGB	$110_{-10}^{+15}$	4.2	100	23
9.0- $M_{\odot}$ SAGB	$110_{-10}^{+15}$	4.1	100	23
15- $M_{\odot}$ CCSN	$94_{-12}^{+19}$	0.44	250	84
19- $M_{\odot}$ CCSN	$120_{-13}^{+18}$	0.74	430	61
20- $M_{\odot}$ CCSN	$71_{-9}^{+15}$	0.22	130	130
21- $M_{\odot}$ CCSN	$59_{-8}^{+13}$	0.14	80	170
25- $M_{\odot}$ CCSN	$130_{-13}^{+17}$	0.98	570	52
8-10- $M_{\odot}$ ECSN	$67_{-8}^{+12}$	0.61	351	43

*Errors are only for variances in the Knie et al. (2004) decay-corrected fluence value and do not include variations in nuclear reaction rates (SNe) or delayed super-wind phase (SAGBs). These parameters are calculated with the Fe uptake factor,  $U_{\text{Fe}} = 0.5$ .*

## 6.2. Thermonuclear Supernovae

TNSN produce so little  $^{60}\text{Fe}$  that it would require a TNSN to have been at a distance of  $\sim 0.6$  pc in order to produce the signal measured by Knie et al. (2004). This is an implausibly short distance, and any uncertainty in the fluence measurement would not change this determination. At that range, the TNSN would have killed nearly all life on Earth, so we can exclude a TNSN as the source of the  $^{60}\text{Fe}$  signal (in this case, the descreening kill distance for a TNSN is  $\sim 10$  pc and the ionizing radiation kill distance from  $10^{48}$  ergs of  $\gamma$ -rays is  $\sim 20$  pc, Smith et al. 2004). Adopting the largest yield ( $M_{\text{ej},^{60}\text{Fe}} \sim 10^{-7} M_{\odot}$ ) from Seitzzahl et al. (2013) extends the distance to  $\sim 6$  pc, which is still inside the kill radius and does not change this conclusion.

## 6.3. Kilonovae

Our calculations give a possible KN distance of  $\sim 5$  pc. Of the little that is known observationally or even theoretically about KNe, we are unaware of any estimates of their ionizing radiation output. In addition, the strength and shape of the shock from ejected material is highly dependent on the orientation of the merger. Thus, we are unable to estimate the corresponding kill distance either by direct exposure or descreening. The ejecta from KNe are certainly energetic (explosive velocities  $\sim 0.3c$ , Goriely et al. 2011), and one might imagine decompressing neutron star matter initially emitting in the UV or at shorter wavelengths. However, the observed radiation for the KN candidate associated with GRB 130603B is very red at times  $\gtrsim 8$  hours (Berger et al. 2013). Moreover, while the KN shock and radiation is expected to be much more isotropic than the GRB, more study of the geometry of the resulting blast is needed to determine a definitive kill distance like that used for TNSN. Consequently, a biohazard argument cannot rule out a KN explosion as the source of the  $^{60}\text{Fe}$  anomaly.

However, a much better discriminator for a KN source would be the  $^{244}\text{Pu}/^{60}\text{Fe}$  ratio. The single  $^{244}\text{Pu}$  atom detected by Wallner et al. (2000, 2004) yields a surface fluence of  $3 \times 10^4$  atoms  $\text{cm}^{-2}$  for the period 1 – 14 Myr ago. Looking at the yields from Goriely et al. (2011) again, we can infer the yield for  $A = 244$  should be at least on the order of the yield for  $A = 60$  (i.e.,  $(^{244}\text{Pu}/^{60}\text{Fe})_{\text{KN}} \geq 1$ ).<sup>7</sup> Based on this assumption and the surface fluence for  $^{60}\text{Fe}$  during the signal passing ( $1.41 \times 10^6$  atoms  $\text{cm}^{-2}/0.5 = 3 \times 10^6$  atoms  $\text{cm}^{-2}$ ), then:

$$(^{244}\text{Pu}/^{60}\text{Fe})_{\text{measured}} \approx 10^{-2} \ll 1 \lesssim (^{244}\text{Pu}/^{60}\text{Fe})_{\text{KN predicted}}$$

even though  $^{244}\text{Pu}$  was measured over 10 times the time period as  $^{60}\text{Fe}$  (Note: this assumes the dust fraction for Pu is the same as Fe,  $f_{\text{Pu}} \sim f_{\text{Fe}}$ ).

Additionally, KN occur infrequently ( $\sim 10 \text{ Myr}^{-1} \text{ galaxy}^{-1}$ , Goriely et al. 2011) compared to CCSN & ECSN ( $\sim 30 \text{ kyr}^{-1} \text{ galaxy}^{-1}$ ).<sup>8</sup> If we approximate the Milky Way as a thin cylinder of radius 10 kpc and thickness 200 pc, the rates ( $\Gamma$ ) of a KN occurring within  $\sim 5$  pc or a CCSN/ECSN occurring within  $\sim 75$  pc of the Earth are:

$$\begin{aligned} \Gamma_{\text{nearby source}} &= \Gamma_{\text{galaxy}} \frac{V_{\text{nearby source}}}{V_{\text{galaxy}}} \\ \Gamma_{\text{nearby KN}} &= \left( \frac{1}{10^7 \text{ Myr}} \right) \left( \frac{D}{5 \text{ pc}} \right)^3 \\ \Gamma_{\text{nearby SN}} &= \left( \frac{1}{1 \text{ Myr}} \right) \left( \frac{D}{75 \text{ pc}} \right)^3 \end{aligned}$$

After inverting these quantities, we can expect a nearby SN every  $\sim 1$  Myr compared to a nearby KN every  $\sim 10^7$  Myr  $\gg 1/H_0$  (the Hubble time). This makes a KN an unlikely source for the  $^{60}\text{Fe}$  signal. However, this result should be revisited as specific yields for  $^{60}\text{Fe}$  become available and especially if a signal from strong  $r$ -process isotopes is detected (e.g.,  $^{146}\text{Sm}$ ,  $^{182}\text{Hf}$ , and  $^{244}\text{Pu}$ ).

#### 6.4. Super-AGB Stars

Figure 3 plots three of our six examined SAGBs (all are listed in Table 3). Their distances range  $\sim 60 - 110$  pc; similar to those of CCSNe. With errors, all SAGBs lie well within the distance for dust stopping due to drag ( $\sim 90$  kpc) but well outside the magnetic deflection distance ( $\sim 1$  pc). While it is tempting to rule out SAGBs as a source under the assumption that any dust would be quickly deflected, we have decided to not rule out SAGBs (see, e.g., Frisch 1995; Cox & Helenius 2003; Florinski et al. 2004; Frisch et al. 2012) since there is uncertainty in the strength, direction, and uniformity of the Local Bubble’s magnetic field. Depending on the nature of the Local Bubble’s magnetic field, charged dust particles could travel with very little deflection. Instead, we will be examining an alternate search in a future work.

---

<sup>7</sup>More likely,  $A = 244$  yields are 10-100 times larger than  $A = 60$  yields given the  $A \sim 240$  yields and the fact that the fission recycling sources are centered around  $A \simeq 280 - 290$  region, Goriely et al. (2011).

<sup>8</sup>We would like to thank the reviewer for suggesting this addition to the KNe discussion.

### 6.5. $^{26}\text{Al}$ Results

In Figure 4, we plot  $^{26}\text{Al}$  predictions for various progenitors, and the expected background in the Accelerator Mass Spectrometry (AMS) data from Feige et al. (2013) using the same 3-kyr sampling intervals used in this experiment. Because  $f_{\text{Al,SN}} \approx 0$ , we do not expect any signal to be present if the source were a SN. The calculated signal from a  $15-M_{\odot}$  CCSN with  $f_{\text{Al,SN}} = 1$  is plotted simply as an example if the dust fraction was significantly higher. Additionally, while we would expect some Al from SAGBs to reach Earth, it would not be visible above the variations in the  $^{26}\text{Al}$  background.

### 6.6. $^{53}\text{Mn}$ Results

In anticipation of AMS  $^{53}\text{Mn}$  measurements mentioned by Feige et al. (2013), in Figure 5 we plot predictions for  $^{53}\text{Mn}$  based on the distance determined by the  $^{60}\text{Fe}$  fluence. Since the survival and grain size for Mn from a SN has not been described to our knowledge, we plotted a range of SN progenitors (since SAGBs are not expected to produce  $^{53}\text{Mn}$ ) and dust fractions, using the largest possible signal source ( $21-M_{\odot}$  CCSN), a mid-range source ( $15-M_{\odot}$  CCSN), and the lowest source (ECSN). We varied the dust fraction from an order of magnitude above to an order of magnitude below  $f_{\text{SN,Fe}}$ . As can be seen for the 15- and  $21-M_{\odot}$  CCSN with  $f_{\text{SN,Mn}} \gtrsim f_{\text{SN,Fe}}$ , a signal should be readily detectable the given the AMS detection threshold of  $\sim 10^{-15}$   $^{53}\text{Mn}/^{55}\text{Mn}$  (Poutivtsev et al. 2010). However, for the ECSN and most CCSNe with  $f_{\text{SN,Mn}} < f_{\text{SN,Fe}}$  (even a  $21-M_{\odot}$  case could be difficult to detect depending on the fluctuations in the  $^{53}\text{Mn}/^{55}\text{Mn}$  background), it should be improbable for a SN progenitor to be detected with  $^{53}\text{Mn}$ .

## 7. Discussion and Conclusions

Since the discovery and confirmation of the terrestrial  $^{60}\text{Fe}$  signal by Knie et al. (1999) and Knie et al. (2004), several experiments have tried to find a corroborating signal either in lunar samples or with other isotopes. To date, none of these experiments provided a definitive signal on the order of that originally reported. This paper attempts to provide a context for these observations and seek other possible progenitors besides a CCSN whose properties could be consistent with the observations. We also anticipate future observations with a hope for time-resolved signals.

From our list of candidates, we can rule out a TNSN as it would be too close ( $\sim 0.6$  pc) to both create the  $^{60}\text{Fe}$  signal and to not kill most life on Earth. We also rule out a KN as a potential source. The KN would have been  $\sim 5$  pc away from the Earth, and while more study of the geometry of a KN is required to determine a definitive kill distance, the low amount of  $^{244}\text{Pu}$  (a strong  $r$ -process element) detected to date contrasted with the high number of  $r$ -process elements per merger makes a KN a low probability. Additionally, KNe/Neutron Star Mergers are very rare, making it unlikely for the Solar System to have passed within 5 pc of one.

Although SAGB stars are outside the magnetic field deflection distance, we have decided to not rule out SAGB stars based solely on this stipulation. Depending on the strength, direction, and uniformity of the Local Bubble’s magnetic field and the charge on the dust grains, it may be possible for a SAGB to have produced the measured  $^{60}\text{Fe}$  signal. Since a SAGB would likely have evolved to the white dwarf stage by now, we plan to investigate this possibility in a future work.

All variations of CCSNe and ECSN remain possible sources. Of these, ECSN would be the most



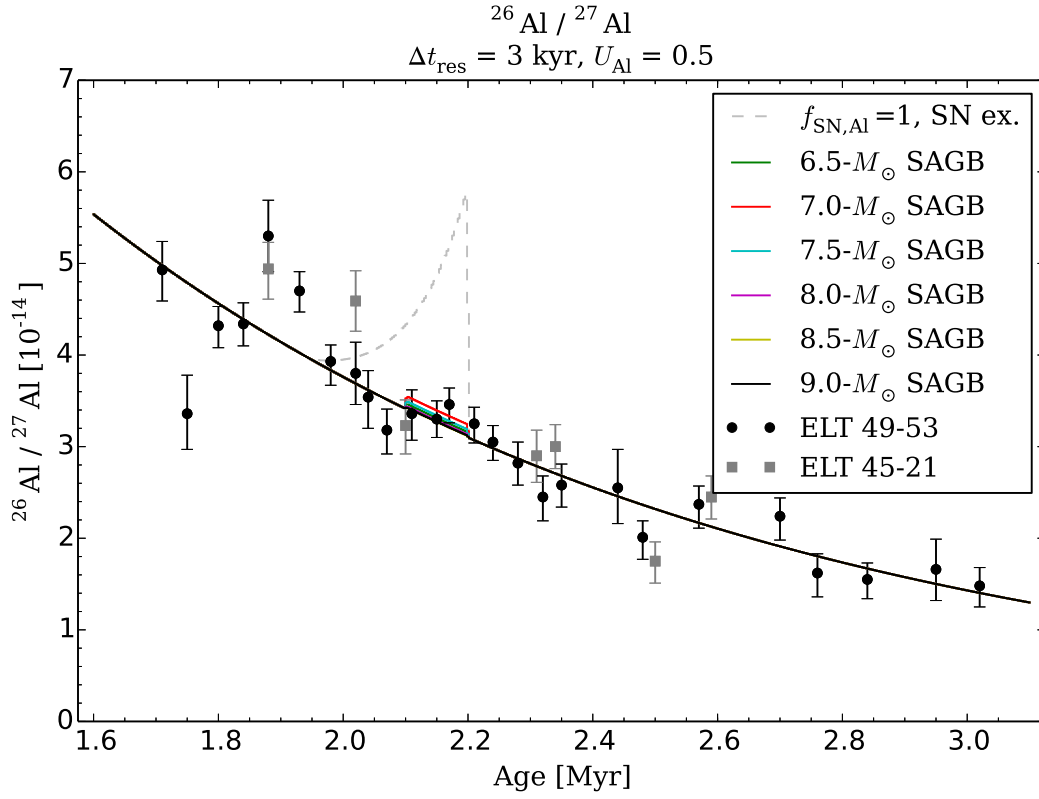


Fig. 4.— Model predictions compared with the  $^{26}\text{Al}$  AMS data from Feige et al. (2013). Note that the  $15-M_{\odot}$  SN is an example only and included to demonstrate the consequence if  $f_{\text{SN,Al}} = 1$  instead of the  $f_{\text{SN,Al}} \sim 0$  we expect.

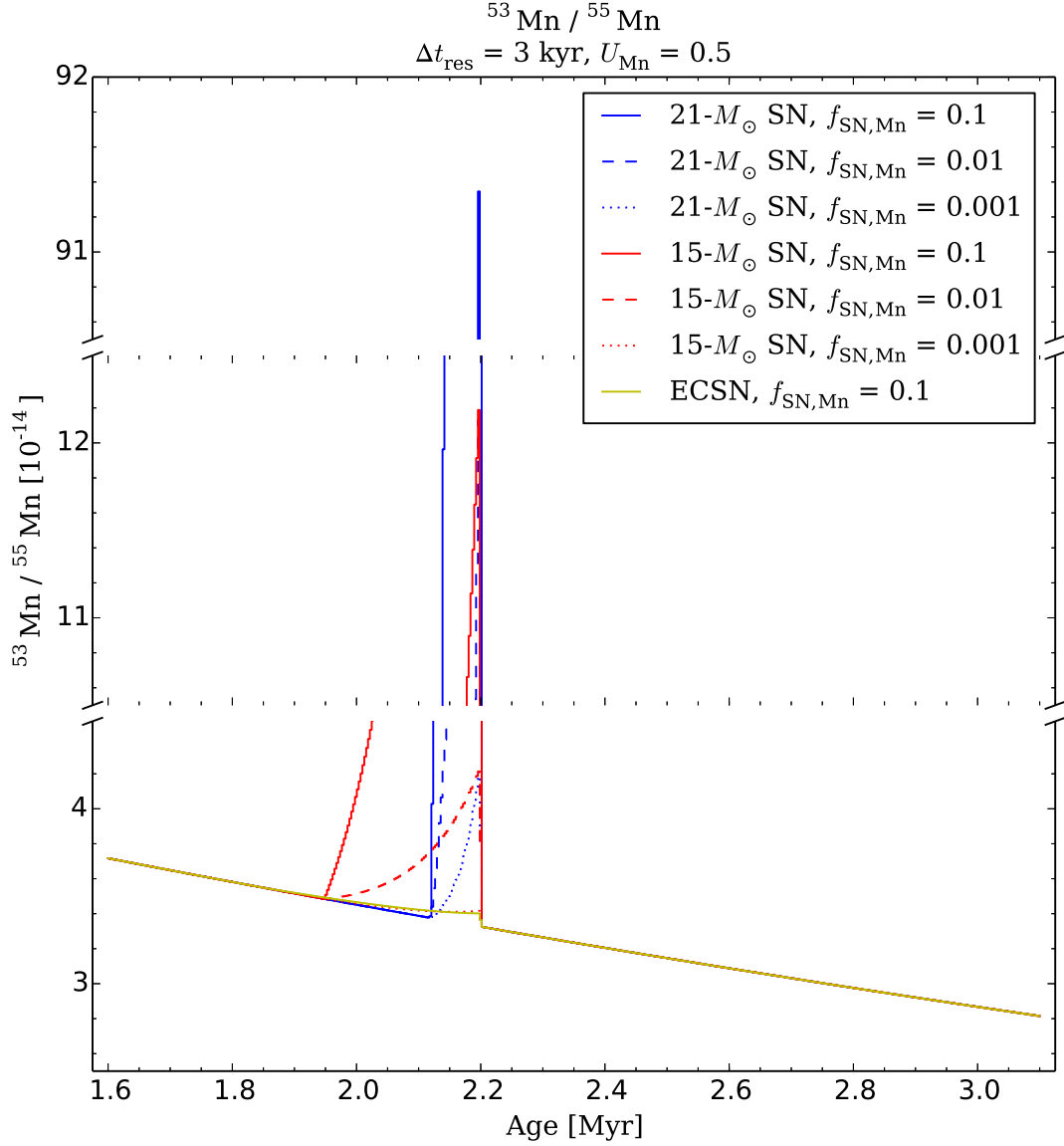


Fig. 5.— Model predictions for upcoming  $^{53}\text{Mn}$  AMS measurements. The vertical axis has been broken into three parts in order to show the peak values of each configuration. Note that the average background  $^{53}\text{Mn}/^{55}\text{Mn}$  level (Feige et al. 2013) is shown ahead of the SN’s arrival. With an AMS sensitivity of  $\sim 10^{-15}$   $^{53}\text{Mn}/^{55}\text{Mn}$  (Poutivtsev et al. 2010), progenitors such as a 21- $M_{\odot}$  SN should be detectable across a range of  $f_{\text{SN,Mn}}$  values, whereas an ECSN progenitor should not be detectable.

likely, firstly, because they arise from the lowest-mass and thus most common core-collapse progenitors. Additionally, Fuchs et al. (2006) listed members of the Sco-Cen association and their masses (using their listed magnitudes and mass-to-magnitude relation) which included the range:  $M_{\text{Sco-Cen}} = 2.5 - 8.2 M_{\odot}$ , compared to  $M_{\text{ECSN}} = 8 - 10 M_{\odot}$ . Since more massive stars evolve faster than lower-mass stars, it is reasonable to expect the signal progenitor to be near the upper end of the mass range. Lastly, the continued lack of a definitive  $^{244}\text{Pu}$  signal, in spite of multiple attempts, is also consistent with the possibility of an ECSN as the progenitor due to its lack of strong  $r$ -process products.

Several caveats are important to bear in mind. Probably most importantly, our ability to test different explosion candidates is only as good as the radioactive yield predictions. These challenging calculations are continually improving, but are subject to significant uncertainties, including stellar evolution, hydrodynamics, and nuclear physics. Indeed, two key nuclear cross sections alone can lead to  $^{60}\text{Fe}$  and  $^{26}\text{Al}$  yield variations by factors up to  $\sim 10$  (Tur et al. 2010). This alone suggests that all of the CCSN candidates should be revisited as yields improve. Seitzzahl et al. (2013) showed that TNSN yields are sensitive to the number of initiation sites and the transition from deflagration to detonation. Clearly, improved radioisotope yield calculations for any of our explosive sources could dramatically change the landscape of possible scenarios. Thus, we implore future nucleosynthesis studies to include (at least)  $^{60}\text{Fe}$  and the other radioisotopes we have discussed here.

Other important uncertainties similarly invite future work. As we have seen, Fe uptake in Fe-Mn crusts represent another topic that invites future study. Uptake has a dramatic impact on our results: the inferred distance to the explosion scales as  $D \propto U_i^{1/2}$ . Additionally, the local interstellar density and magnetic field plays a key role in the propagation of the signal (whether from a SN or SAGB) and in the duration of the time profile of the radioisotope flux. Finally, as we have seen, the observability of different radioisotopes is highly sensitive on the formation and survival of supernova dust of different compositions and sizes. We have relied on theoretical calculations (Silvia et al. 2010, 2012) which imply, among other things, that  $^{26}\text{Al}$  is unlikely to be observable terrestrially despite its SN abundance comparable to  $^{60}\text{Fe}$ . Further such theoretical studies relevant to other radioisotopes, and observational corroboration, are critically needed.

To confirm the origin of the  $^{60}\text{Fe}$  signal and pin down its source will require measurements of  $^{60}\text{Fe}$  at other sites, other sources (e.g., magnetosomes in addition to crust and sediment), and other radioisotopes. Lunar regolith measurements provide unique confirmation of the terrestrial  $^{60}\text{Fe}$  signal. However, we find absolute measurements will be difficult because high-velocity dust vaporizes on the lunar surface and much of the incident material will then escape the Moon. This said, we eagerly await detailed presentation of lunar measurements hinted at by Fimiani et al. (2014). We are also looking forward to  $^{53}\text{Mn}$  measurements as mentioned by Feige et al. (2013) and  $^{244}\text{Pu}$  measurements by Piran et al. (2014, see Wallner, et al. 2014, citation therein) that will be helpful in discriminating between the remaining possible progenitors.

Looking ahead to further measurements, the behavior of dust condensation, survival, and filtering will be a key factor in narrowing the remaining pool of possible progenitors. The dust fraction includes several filtering processes that can all affect the resulting distance calculation ( $D \propto f_i^{1/2}$ ). Studies of dust formation have focused on silicates, iron, and corundum, but formation processes with other elements (especially Mn, Ca, Ti, Zr, Tc, and Pu) could be used to differentiate the remaining possibilities given the varying yield ratios between these elements for each progenitor. The search for other isotopes is not simply a matter of choosing those with high lifetimes ( $\tau_i \sim \mathcal{O}(\text{Myr})$ ), but also those with low backgrounds, high condensation temperatures (in order to form dust grains), and large grain sizes ( $a \gtrsim 0.2 \mu\text{m}$ ). Of particular interest would be  $^{41}\text{Ca}$  and  $^{53}\text{Mn}$ . While perhaps not ideal candidates with regards to background levels, they have long lifetimes and can be condensed at high temperatures ( $\gtrsim 1100 \text{ K}$ ) into Perovskite ( $\text{CaTiO}_3$ ), Melilite

( $\text{Ca}_2\text{Al}_2\text{SiO}_7$ ,  $\text{Ca}_2\text{MgSi}_2\text{O}_7$ ), and Alabandite ( $\text{MnS}$ ) (see Field 1975). Other possible isotopes with long lifetimes such as  $^{93}\text{Zr}$ ,  $^{97}\text{Tc}$ ,  $^{99}\text{Tc}$ , and  $^{107}\text{Pd}$ , as well as strong  $r$ -process elements such as  $^{146}\text{Sm}$ ,  $^{182}\text{Hf}$  and  $^{244}\text{Pu}$  could be used to constrain CCSNe if more details of their dust condensation are determined, but, regardless, any other candidate isotope would need to form grains large enough to survive escape from its progenitor and enter the Solar System. It would be a remarkable coincidence if the only isotope that is capable of carrying an extra-solar signal (i.e.,  $^{60}\text{Fe}$ ) is the first one examined.

With observations of additional isotopes, it is possible not only to identify a specific event or progenitor, but also to: (1) provide a better measure of the distance to the source, (2) directly probe individual radioisotope nucleosynthesis, (3) constrain the nearby SN rate, (4) guide astrophysical searches for the SN remains (i.e., pulsars), and (5) model the explosion light curve and to assess the possible damage to the terrestrial biosphere. Finally, we have seen that the measurement of time-resolved radioisotope profiles provides direct information of the blast passage through the Solar System and an independent measurement of the distance to the progenitor. The authors are optimistic that new data will make such questions tractable in the near future.

Since our first submission, we have been made aware of the superb thesis by Jenny Feige that covers many similar topics and was completed independently of this work (Feige 2010). We are pleased to acknowledge the Vera Laboratory including Jenny Feige, as well as the Technische Universität München (TUM) Group including Shawn Bishop. We would also like to thank our reviewer whose thoughtful and thorough comments on the manuscript greatly improved this work. We are grateful to Thomas Johnson and Craig Lundstrom for illuminating discussions of isotope geology. The work of John Ellis was supported partly by the London Centre for Terauniverse Studies (LCTS), using funding from the European Research Council via the Advanced Investigator Grant 267352. Brian Fields thanks Stuart Shapiro for his enlightening discussions about the Sedov solution and Friedrich-Karl Thielemann and Ivo Seitenzahl for their informative discussions of supernova radionuclide synthesis.

## REFERENCES

- Abt, H. A. 2011, *AJ*, 141, 165
- Adams, S. M., Kochanek, C. S., Beacom, J. F., Vagins, M. R., & Stanek, K. Z. 2013, *ApJ*, 778, 164
- Alvarez, L., Alvarez, W., Asaro, F., & Michel, H. 1980, *Sci*, 208, 4448, 1095-1108
- Ammosov, A. E., Berezhko, E. G., Konstantinov, A. N., et al. 1991, *Akademiia Nauk SSSR Izvestiia Serii Fizicheskaiia*, 55, 2037
- Athanassiadou, T. & Fields, B. D. 2011, *NewA*, 16, 4, 229-241
- Atri, D., & Melott, A. L. 2014, *Astroparticle Physics*, 53, 186
- Beech, M. 2011, *Ap&SS*, 336, 287
- Benítez, N., Maíz-Apellániz, J., & Canelles, M. 2002, *Physical Review Letters*, 88, 081101
- Berger, E., Fong, W., & Chornock, R. 2013, *ApJ*, 774, LL23
- Berghöfer, T. W. & Breitschwerdt, D. 2002, *A&A*, 390, 299-306
- Bignami, G. F., & Caraveo, P. A. 1996, *ARA&A*, 34, 331
- Bishop, S. & Egli, R. 2011, *Icarus*, 212, 2, 960-962
- Book, D. L. 1994, *Shock Waves*, 4, 1, 1-10
- Burns, J.A., Lamy, P.L., & Soter, S. 1979, *Icarus*, 40, 1
- Chu, Y.-H. 2008, *IAUS*, 250, 341-354
- Cintala, M. J. 1992, *J. Geophys. Res.*, 97, 947-973
- Collette, A., Sternovsky, Z., & Horanyi, M. 2014, *Icarus*, 227, 89-93
- Cook, D. L., Berger, E., Faestermann, T., et al. 2009, *LPI*, 40, 1129
- Cox, D. P., & Helenius, L. 2003, *ApJ*, 583, 205
- Cremonese, G., Borin, P., Lucchetti, A., Marzari, F., & Bruno, M. 2013, *A&A*, 551, A27
- Dartnell, L. R. 2011, *Astrobiology*, 11, 551
- Doherty, C. L., Gil-Pons, P., Lau, H. H. B., Lattanzio, J. C., & Siess, L. 2014, *MNRAS*, 437, 1, 195-214
- Draine, B. T., & Salpeter, E. E. 1979, *ApJ*, 231, 77
- Draine, B. T. 2011, *Physics of the Interstellar and Intergalactic Medium*. Princeton University Press, 2011. ISBN: 978-0-691-12214-4
- Ellis, J., Fields, B. D., & Schramm, D. N. 1996, *ApJ*, 470, 1227
- Ellis, J., & Schramm, D. N. 1995, *Proceedings of the National Academy of Science*, 92, 235
- Ejzak, L. M., Melott, A. L., Medvedev, M. V., & Thomas, B. C. 2007, *ApJ*, 654, 373

- Faherty, J., Walter, F. M., & Anderson, J. 2007, *Ap&SS*, 308, 225
- Feige, Jenny. “The connection between the local bubble and the  $^{60}\text{Fe}$  anomaly in the deep sea hydrogenetic ferromanganese crust.” Master’s thesis, University of Vienna, 2010. <http://othes.univie.ac.at/8920/>
- Feige, J., Wallner, A., Winkler, S. R., et al. 2012, *PASA*, 29, 2, 109-114
- Feige, J., Wallner, A., Fifield, L. K., et al. 2013, *EPJWC*, 63, 03003
- Field, G. B. 1975, *The Dusty Universe*, 89
- Fields, B. D. 2004, *New A Rev.*, 48, 119
- Fields, B. D., & Ellis, J. 1999, *NewA*, 4, 6, 419-430
- Fields, B. D., Hochmuth, K. A., & Ellis, J. 2005, *ApJ*, 621, 2, 902-907
- Fields, B. D., Athanassiadou, T., & Johnson, S. R. 2008, *ApJ*, 678, 1, 549-562
- Fimiani, L., Cook, D. L., Faestermann, T., et al. 2012, *LPI*, 43, 1279
- Fimiani, L., Cook, D. L., Faestermann, T., et al. 2014, *LPI*, 45, 1778
- Fitoussi, C., Raisbeck, G. M., Knie, K., et al. 2008, *PhRvL*, 101, 12, 121101
- Florinski, V., Pogorelov, N. V., Zank, G. P., Wood, B. E., & Cox, D. P. 2004, *ApJ*, 604, 700
- Frisch, P. C. 1995, *Space Sci. Rev.*, 72, 499
- Frisch, P. C., Andersson, B.-G., Berdyugin, A., et al. 2012, *ApJ*, 760, 106
- Fuchs, B., Breitschwerdt, D., de Avillez, M. A., Dettbarn, C., & Flynn, C. 2006, *MNRAS*, 373, 3, 993-1003
- Fujita, Y., Ohira, Y., & Takahara, F. 2010, *ApJ*, 712, L153
- Gehrels, N., Laird, C. M., Jackman, C. H., et al. 2003, *ApJ*, 585, 1169
- Goriely, S., Bauswein, A., & Janka, H.-T. 2011, *ApJ*, 738, 2, L32
- Gustafson, B.A.S. 1994, *Annual Review of Earth and Planetary Sciences*, 22, 553
- Hoppe, P., & Zinner, E. 2000, *J. Geophys. Res.*, 105, 10371
- Knie, K., Korschinek, G., Faestermann, T., et al. 1999, *PhRvL*, 83, 1, 18-21
- Knie, K., Korschinek, G., Faestermann, T., et al. 2004, *PhRvL*, 93, 17, 171103
- Langevin, Y., & Arnold, J. R. 1977, *AREPS*, 5, 449-489
- Lattimer, J. M., & Schramm, D. N. 1974, *ApJ*, 192, L145
- Li, L.-X., & Paczyński, B. 1998, *ApJ*, 507, L59
- Limongi, M., & Chieffi, A. 2006, *ApJ*, 647, 1, 483-500
- Linde, T.J., & Gombosi, T.I. 2000, *J. Geophys. Res.*, 105, 10411

- Looney, L. W., Tobin, J. J., & Fields, B. D. 2006, *ApJ*, 652, 1755
- Mathis, J.S., Rumpl, W., & Nordsieck, K.H. 1977, *ApJ*, 217, 425
- Matsuura, M., Dwek, E., Meixner, M., et al. 2011, *Sci*, 333, 6047, 1258-1261
- McCullough, P. R., Fields, B. D., & Pavlidou, V. 2002, *ApJ*, 576, L41
- Melott, A. L., & Thomas, B. C. 2011, *Astrobiology*, 11, 343
- Metzger, B. D., Martínez-Pinedo, G., Darbha, S., et al. 2010, *MNRAS*, 406, 2650
- Meynadier, L., Valet, J.-P., Bassinot, F. C., Shackleton, N. J., & Guyodo, Y. 1994, *E&PSL*, 126, 109-127
- Murray, N., Weingartner, J.C., & Capobianco, C. 2004, *ApJ*, 600, 804
- Nava, D. F., & Philpotts, J. A. 1973, *Ge Co A*, 37, 4, 963-973
- Nishiizumi, K., Imamura, M., Kohl, C. P., et al. 1979, *E&PSL*, 44, 3, 409-419
- Nishiizumi, K., Arnold, J. R., Kubik, P. W., & Sharma, P. 1990, *LPI*, 21, 895
- Nomoto, K., Thielemann, F.-K., & Yokoi, K. 1984, *ApJ*, 286, 644-658
- Paul, M., Valenta, A., Ahmad, I., et al. 2001, *ApJ*, 558, 2, L133-L135
- Paul, M., Valenta, A., Ahmad, I., et al. 2003, *NuPhA*, 719, C29-C36
- Paul, M., Valenta, A., Ahmad, I., et al. 2007, *J. Radioanal Nucl Chem.*, 272, 2, 243-245
- Piran, T., Korobkin, O., & Rosswog, S. 2014, arXiv:1401.2166
- Pollack, J.B., Hollenbach, D., Beckwith, S., et al. 1994, *ApJ*, 421, 615
- Poutitsev, M., Dillmann, I., Faestermann, T., et al. 2010, *NIMPB*, 268, 7-8, 756-758
- Raisbeck, G. M., Yiou, F., Bourles, D., Lorius, C., & Jouzel, J. 1987, *Nature*, 326, 273
- Raisbeck, G., Tran, T., Lunney, D., et al. 2007, *NIMPB*, 259, 1, 673-676
- Rauscher, T., Heger, A., Hoffman, R. D., & Woosley, S. E. 2002, *ApJ*, 576, 1, 323-348
- Rho, J., Kozasa, T., Reach, W.T., et al. 2008, *ApJ*, 673, 271
- Ruderman, M. A. 1974, *Science*, 184, 1079
- Seitenzahl, I. R., Ciaraldi-Schoolmann, F., Röpke, F. K., et al. 2013, *MNRAS*, 429, 1156
- Spitzer, L., Jr., & Jenkins, E. B. 1975, *ARA&A*, 13, 133-164
- Shklovskii, I. S., & Sagan, C. 1966, *Intelligent life in the universe* by I. S. Shklovskii [and] Carl Sagan. Authorized translation by Paula Fern. San Francisco: Holden-Day, 1966.
- Shklovskij, I. S. 1969, *Supernovae* (New York, NY: Interscience Publishers)
- Shu, F. H. 1992, *The physics of astrophysics. Volume II: Gas dynamics.*, by Shu, F.H. University Science Books, Mill Valley, CA (USA), 1992, ISBN 0-935702-65-2

- Siess, L. 2010, *A&A*, 512, A10
- Silvia, D.W., Smith, B.D., & Shull, J.M. 2010, *ApJ*, 715, 1575
- Silvia, D.W., Smith, B.D., & Shull, J.M. 2012, *ApJ*, 748, 12
- Slavin, J. D., Frisch, P. C., Heerikhuisen, J., et al. 2010, Twelfth International Solar Wind Conference, 1216, 497
- Smith, D. S., Scalo, J., & Wheeler, J. C. 2004, *Icarus*, 171, 229
- Sterken, V.J., Altobelli, N., Kempf, S., et al. 2013, *A&A*, 552, A130
- Symbalisty, E., & Schramm, D. N. 1982, *Astrophys. Lett.*, 22, 143
- Tanvir, N. R., Levan, A. J., Fruchter, A. S., et al. 2013, *Nature*, 500, 547
- Tetzlaff, N., Torres, G., Neuhäuser, R., & Hohle, M. M. 2013, *MNRAS*, 435, 879
- Thomas, B. C., Melott, A. L., Field, B. D., & Anthony-Twarog, B. J. 2008, *Astrobiology*, 8, 9
- Tur, C., Heger, A., & Austin, S. M. 2010, *ApJ*, 718, 357
- Ventura, P., Criscienzo, M. Di, Schneider, R., et al. 2012, *MNRAS*, 424, 3, 2345-2357
- Wallner, C., Faestermann, T., Gerstmann, U., et al. 2000, *NIMPB*, 172, 1-4, 333-337
- Wallner, C., Faestermann, T., Gerstmann, U., et al. 2004, *NewAR*, 48, 1-4, 145-150
- Wanajo, S., Nomoto, K., Janka, H. T., Kitaura, F. S., & Müller, B. 2009, *ApJ*, 695, 208
- Wanajo, S., Janka, H.-T., & Müller, B. 2013, *ApJ*, 774, 1, L6
- Wasserburg, G. J., Busso, M., Gallino, R., & Nollett, K. M. 2006, *NuPhA*, 777, 5-69
- Weingartner, J.C., & Draine, B.T. 2001, *ApJ*, 548, 296
- Zel'dovich, Y. B., & Raizer, Y. P. 1967, New York: Academic Press, 1966/1967, edited by Hayes, W.D.;  
Probstein, Ronald F.,



### A. List of Variables

Variable	- Description [common value or unit of measure]
$a$	- radius of dust grain [ $\mu\text{m}$ ]
$A$	- atomic number [dimensionless]
$\alpha$	- signal width parameter [ $\approx 0.577$ ]
$\beta$	- ratio of Sun's radiation force to gravitational force on a particle [dimensionless]
$c$	- speed of light [ $\sim 3 \times 10^5 \text{ km s}^{-1}$ ]
$c_s$	- speed of sound in ISM [ $\text{km s}^{-1}$ ]
$C_r$	- constant from combination of solar flux, gravitational constant, among others [ $7.6 \times 10^{-5} \text{ g cm}^{-2}$ ]
$D$	- distance from progenitor to Earth [pc]
$\delta$	- shell thickness of uniform shell for a SN remnant [dimensionless]
$E_{\text{CCSN}}$	- energy deposited into ejecta by a CCSN [ $\sim 10^{51}$ ergs]
$E_{\text{ECSN}}$	- energy deposited into ejecta by an ECSN [ $\sim 10^{50}$ ergs]
$E_{\text{KN}}$	- energy deposited into ejecta by a KN [ $\sim 10^{49}$ ergs]
$E_{\text{TNSN}}$	- energy deposited into ejecta by a TNSN [ $\sim 10^{51}$ ergs]
$E_{\text{grain}}$	- kinetic energy of dust grain [ergs]
$E_{\text{vapor}}$	- thermal and kinetic energy in vapor [ergs]
$\epsilon$	- shell thickness of saw-tooth shell [dimensionless]
$f$	- dust fraction, fraction of isotope that passes from progenitor to Earth [dimensionless]
$F_{\text{drag}}$	- drag force on dust grain [dyne]
$F_g$	- force of gravity on dust grain [dyne]
$F_{\text{mag}}$	- force of magnetic field on dust grain [dyne]
$F_r$	- force from solar radiation pressure on dust grain [dyne]
$\mathcal{F}_{\text{arr},i}$	- decay-corrected (or arrival) fluence of an isotope [ $\text{atoms cm}^{-2}$ ]
$\mathcal{F}_{\text{interstellar},i}$	- total fluence of an isotope across spherical signal front [ $\text{atoms cm}^{-2}$ ]
$\mathcal{F}_{\text{obs},i}$	- observed fluence of an isotope [ $\text{atoms cm}^{-2}$ ]
$\mathcal{F}_{\text{surface},i}$	- total fluence of an isotope regardless of uptake [ $\text{atoms cm}^{-2}$ ]
$\mathbb{F}$	- material flux, fluence per time [ $\text{atoms cm}^{-2} \text{ kyr}^{-1}$ ]
$G(x)$	- density profile function [dimensionless]
$G_0(s)$	- collisional drag function [dimensionless]
$\gamma$	- ratio of specific heats [dimensionless]
$\Gamma$	- progenitor rate [ $\text{Myr}^{-1}$ ]
$H_0$	- Hubble Constant [ $\sim 70 \text{ km s}^{-1} \text{ Mpc}^{-1}$ ]
$i$	- (as subscript) 'for a given isotope' (e.g., $^{60}\text{Fe}$ , $^{26}\text{Al}$ , etc.)
$k$	- Boltzmann constant [ $1.38 \times 10^{-16} \text{ erg K}^{-1}$ ]
$m$	- mass [g]
$M$	- mass of progenitor [ $M_{\odot}$ ]
$M_{\text{ej},i}$	- total mass of an isotope in the ejecta [ $M_{\odot}$ ]
$m_u$	- atomic mass unit [ $\sim 1.66 \times 10^{-24} \text{ g}$ ]
$n$	- number density (e.g., of ISM, dust grain, etc.) [ $\text{cm}^{-3}$ ]
$N$	- number of dust grains [dimensionless]
$\mathcal{N}_i$	- number of atoms of an isotope [dimensionless]
$P_{\text{SW}}$	- pressure of solar wind [ $\text{dyne cm}^{-2}$ ]
$Q_{\text{pr}}$	- efficiency of solar radiation on dust grain [dimensionless]
$R_{\text{drag}}$	- distance at which drag effects are significant on a dust grain [pc]

- $R_{\text{fade}}$  - distance at which a SN shock transitions into a sound wave [pc]  
 $R_{\text{kill}}$  - distance from the Sun a SN progenitor can produce a shock that penetrates to Earth's orbit [pc]  
 $R_{\text{mag}}$  - distance at which magnetic deflection effects are significant on a dust grain [pc]  
 $R_{\text{SAGB}}$  - radius of leading edge of SAGB dust shell [pc]  
 $R_{\text{SN}}$  - radius of leading edge of SN remnant [pc]  
 $\rho$  - mass density (e.g., of ISM, dust grain, etc.) [ $\text{g cm}^{-3}$ ]  
 $\rho_0$  - density in front of shock [ $\text{g cm}^{-3}$ ]  
 $\rho_1$  - density behind shock [ $\text{g cm}^{-3}$ ]  
 $s$  - velocity parameter [dimensionless]  
 $t$  - elapsed time [Myr]  
 $t_{\text{arr}}$  - time from today in the past that the leading edge of the signal arrived [Myr]  
 $t_{\text{dep}}$  - time from today in the past that the trailing edge of the signal departed [Myr]  
 $t_{\text{travel}}$  - time for isotope to transit from progenitor to Earth [Myr]  
 $T$  - temperature of ISM [K]  
 $T_C$  - condensation temperature [K]  
 $\Delta t_{\text{inter}}$  - delay between envelope pulses of SAGB [ $\sim 100$  yr]  
 $\Delta t_{\text{pulse}}$  - duration of envelope pulse of SAGB [ $\sim 1$  yr]  
 $\Delta t_{\text{res}}$  - time resolution of samples [kyr]  
 $\Delta t_{\text{SAGB}}$  - duration of SAGB phase [ $\sim 100$  kyr]  
 $\Delta t_{\text{signal}}$  - signal width, time for signal to pass Earth and duration of ejecta deposition on Earth [kyr]  
 $\tau_i$  - mean lifetime of an isotope,  $\tau_i = \tau_{1/2,i} / \ln 2$  [Myr]  
 $\tau_{1/2,i}$  - half-life of an isotope [Myr]  
 $U_i$  - uptake, fraction of deposited isotope that is incorporated into sampled material [dimensionless]  
 $v$  - speed [ $\text{km s}^{-1}$ ]  
 $v_{\text{arr}}$  - velocity of a dust grain upon arrival at Earth [ $\text{km s}^{-1}$ ]  
 $v_{\text{esc}}$  - escape velocity [ $\text{km s}^{-1}$ ]  
 $v_{\text{grain}}$  - speed of dust grain/impactor [ $\text{km s}^{-1}$ ]  
 $v_{\text{grain},0}$  - initial speed of dust grain [ $\text{km s}^{-1}$ ]  
 $v_{\infty}$  - speed at infinity [ $\text{km s}^{-1}$ ]  
 $v_{\text{SN}}$  - speed of leading edge of the SN remnant [ $\text{km s}^{-1}$ ]  
 $V$  - volume [ $\text{cm}^3$ ]  
 $\mathcal{V}$  - voltage of dust grain [V]  
 $X$  - mass fraction [dimensionless]  
 $\xi_0$  - SN proportionality constant [dimensionless] (Zel'dovich & Raizer 1967)

$$\xi_0 = \left[ \frac{75}{16\pi} \frac{(\gamma - 1)(\gamma + 1)^2}{(3\gamma - 1)} \right]^{1/5} \stackrel{\gamma=5/3}{\approx} 1.1$$

$\zeta_0$  - SAGB proportionality constant [dimensionless]

$$\zeta_0 = \frac{\sqrt{2\pi\gamma}}{4} \stackrel{\gamma=5/3}{\approx} 0.81$$

## B. Blast Expansion and Radioisotope Flux Profile

We model astrophysical explosions as spherically symmetric, and we are interested in distances sufficiently large that the swept up interstellar mass is much larger than the ejecta mass. We treat a blast wave

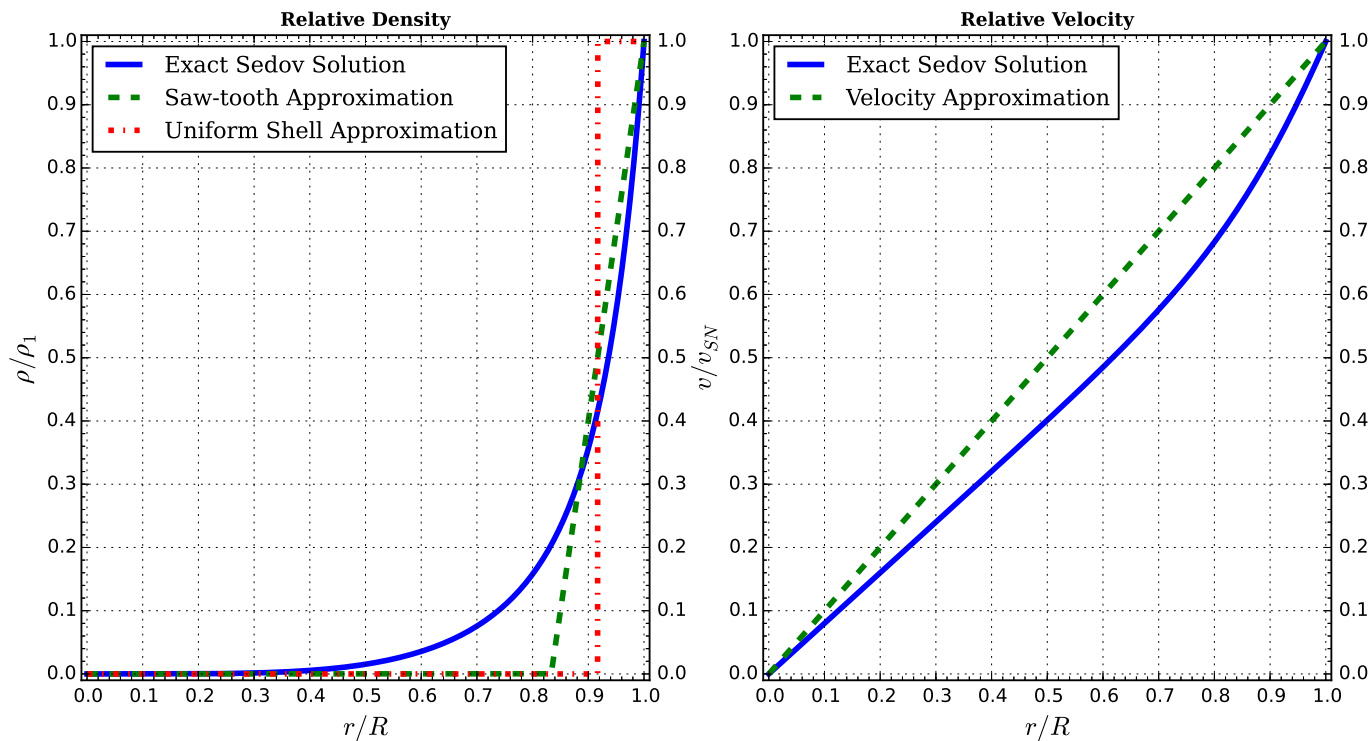


Fig. 6.— Comparison of the uniform shell and saw-tooth profiles to exact solution profile, for  $\gamma = 5/3 \Rightarrow \delta \approx 0.083$  (uniform shell),  $\epsilon \approx 0.17$  (saw-tooth). In addition, the paper used a ratio to approximate the observed SN crossing velocity. The right chart compares this approximation to the exact solution profile.

as adiabatic (energy-conserving) and thus adopt the Sedov-Taylor solution. The Sedov blast wave evolves in a self-similar manner. This means in particular that gas properties as a function of radius  $r$  maintain the same shape when plotted in terms of the similarity variable:

$$x = \frac{r}{R_{\text{SN}}(t)}$$

where the shock radius at  $t$  is given by Equation (2). In particular, the density profile is:

$$\rho(r, t) = \rho_1 G(r/R_{\text{SN}})$$

where the density immediately behind the shock is:

$$\rho_1 = \frac{\gamma + 1}{\gamma - 1} \rho_0$$

and the dimensionless density profile function is thus normalized to  $G(1) = 1$ . Note that mass conservation implies that the total mass  $M_{\text{swept}} = 4\pi\rho_0 R_{\text{SN}}^3/3$  swept up in the blast is equal to the total mass in the blast profile:

$$M_{\text{total}} = 4\pi \int_0^{R_{\text{SN}}} r^2 \rho(r, t) dr = 4\pi\rho_1 R_{\text{SN}}^3 \int_0^1 x^2 G(x) dx$$

and so setting  $M_{\text{total}} = M_{\text{swept}}$  implies that:

$$\int_0^1 x^2 G(x) dx = \frac{\rho_0}{3\rho_1} = \frac{1}{3} \frac{\gamma - 1}{\gamma + 1} \xrightarrow{\gamma=5/3} \frac{1}{12} \quad (\text{B1})$$

We consider two approximations to the full Sedov profile. For a uniform shell approximation, we have  $G(x) = 1$  for  $x \in [1 - \delta, 1]$  and zero otherwise, which gives the location of the inner shell radius via:

$$\frac{1 - (1 - \delta)^3}{3} = \frac{1}{3} \frac{\gamma - 1}{\gamma + 1}$$

and thus:

$$\delta = 1 - \left( \frac{2}{\gamma + 1} \right)^{1/3} \xrightarrow{\gamma=5/3} 0.0914$$

whereas going to first order in  $\delta$  we would find  $\delta = 1/12$ . For a “saw-tooth” approximation, the blast material is in a thin shell with a profile that linearly decreases from a maximum behind the shock to zero at coordinate  $x_0 \equiv 1 - \epsilon$ . Thus we have  $G(x) = Ax + B$ , with the constraints that  $G(1) = 1$  and  $G(x_0) = 0$  at the inner radius, which gives:

$$G(x) = \frac{x - x_0}{1 - x_0} \quad (\text{B2})$$

Choosing  $\gamma = 5/3$ , to first order we find  $\int_0^1 x^2 G(x) dx = \int_{1-\epsilon}^1 x^2 G(x) dx \approx \epsilon/2$ . From Equation (B1) we find the dimensionless shell thickness  $\epsilon \approx 1/6$ , twice the value in the uniform shell. As seen in Figure 6, the saw-tooth density profile more closely matches the exact Sedov density profile compared to the uniform shell profile, making the saw-tooth profile more appropriate for modeling the signal spreading for our SN distances.

The (radial) velocity profile is:

$$v(r, t) = \dot{R}_s U \left( \frac{r}{R_{\text{SN}}} \right)$$

with  $\dot{R}_s$  the shock speed, and the dimensionless velocity profile function normalized to  $U(1) = 1$ . To a good approximation, the velocity is linear, and we will adopt the approximation  $U(x) \approx x$ . This leads to a “Hubble law” relation:

$$v(r, t) \approx \dot{R}_s \frac{r}{R_{\text{SN}}}$$

Figure 6 compares this linear velocity profile with the exact Sedov solution. Our approximation is necessary to maintain the self-similarity of the saw-tooth profile, and, while different than the exact solution, should be sufficient for the region we are most interested in ( $0.8 \leq r/R \leq 1$ ). For a more detailed description of the analytical Sedov solution, see Book (1994).

Turning to the explosive ejecta, we note that if a number  $\mathcal{N}_i$  of atoms of species  $i$  were distributed with *uniform* density at time  $t$ , then the mean number density in  $i$  would be:

$$n_{i,0} = \frac{3}{4\pi} \frac{\mathcal{N}_i}{R_{\text{SN}}^3}$$

We will assume that, at times of interest, the ejecta is well-mixed into the blast wave, with a constant mass fraction at all radii. That is, we assume that the ejecta density profile follows that of the blast itself. This means that the highest ejecta density is just behind the shock, with a value:

$$n_{i,1} = n_i(R_{\text{SN}}) = \frac{\gamma + 1}{\gamma - 1} n_{i,0}$$

and the ejecta density profile is:

$$n_i(r, t) = n_{i,1} G(r/R_{\text{SN}})$$

Combining the ejecta density profile with the “Hubble law” velocity approximation gives the global-averaged ejecta flux onto the surface of the Earth (i.e., 1/4 the interstellar flux, not including radioactive decay), evaluated at distance  $r = D$ :

$$\mathbb{F}_i(D, t) = \frac{1}{4} n_i(D, t) v(D, t) = \mathcal{F}_1 \left( \frac{D}{R_{\text{SN}}} \right)^3 G(D/R_{\text{SN}}) \frac{\dot{R}_s}{R_{\text{SN}}} \quad (\text{B3})$$

with the time-independent prefactor:

$$\mathcal{F}_1 = \frac{3}{16\pi} \frac{\gamma + 1}{\gamma - 1} \frac{M_{\text{ej},i}/m_i}{D^2} \quad (\text{B4})$$

We see here explicitly that a time-resolved flux directly encodes the blast density profile and thus probes the propagation of the radioisotope ejecta from explosion to Earth.

Using our saw-tooth approximation for the blast density profile  $G$  (Equation B2), and using the Sedov result  $\dot{R}_s/R_{\text{SN}} = 2/5t$ , we find a flux profile in time of:

$$\mathbb{F}_i(D, t) = \frac{2\mathcal{F}_1}{5t} \left( \frac{D}{R_{\text{SN}}} \right)^3 \frac{D/R_{\text{SN}}(t) - 1 + \epsilon}{\epsilon} \quad (\text{B5})$$

We note that the leading edge of the blast from an event at distance  $D$  arrives at a time  $t_i$  given by  $D = R_{\text{SN}}(t_{\text{arr}})$ . Thus we can recast  $D/R_{\text{SN}}(t) = (t/t_{\text{arr}})^{-2/5}$  in terms of the initial arrival time. The trailing edge of the shell arrives at time  $t_{\text{dep}}$  given by  $D = (1 - \epsilon)R_{\text{SN}}(t_{\text{dep}})$ . Thus we have  $t_{\text{dep}} = t_{\text{arr}}/(1 - \epsilon)^{5/2}$ .

This means that we can write  $\epsilon = 1 - (t_{\text{arr}}/t_{\text{dep}})^{2/5}$ , and we can express the global-averaged flux time profile as:

$$\mathbb{F}_i(D, t) = \left(\frac{t}{t_{\text{arr}}}\right)^{-11/5} \left[ \frac{(t/t_{\text{arr}})^{-2/5} - (t_{\text{dep}}/t_{\text{arr}})^{-2/5}}{1 - (t_{\text{dep}}/t_{\text{arr}})^{-2/5}} \right] \mathbb{F}_i(D, t_{\text{arr}}) \quad (\text{B6})$$

This is the sum of two power laws in  $t$ , leading to a steep cusp at early times  $t \rightarrow t_{\text{arr}}$  that flattens at late times  $t \rightarrow t_{\text{dep}}$ .